Ultrasonic tensile test and micro-CT defect analysis on alumina 99.5%

Materials & Design 238 (2024) 112680

Contents lists available at ScienceDirect

Materials & Design

journal homepage: www.elsevier.com/locate/matdes

Ultrasonic tensile test and micro-CT defect analysis on alumina 99.5%

A.P. Pagnoncelli *, A. Tridello, D.S. Paolino, L. Peroni

Department of Mechanical and Aerospace Engineering, Politecnico di Torino, Turin 10129, Italy

A B S T R A C T

The ultrasonic tensile test method recently developed by the Authors is applied with the micro-computed tomography technique aiming to correlate the failure-inducing nominal stress in alumina 99.5% with the manufacturing defect size. After characterizing the defect population, the critical defect size of each specimen is defined, and an empirical formulation for the stress intensity factors on this material is obtained.

The ultrasonic tensile test, with a loading frequency of 20 kHz, is simulated with finite element analyses, to estimate with an optimization process the material properties that reproduce the experimental displacements. Evidence of negligible fatigue damage is verified to further support the validity of the ultrasonic tensile test as a method capable of providing a good estimate for the quasi-static tensile strength.

The analysed alumina resulted in a density of 3969 kg/m^3 and an elastic modulus of 371.2 GPa. All specimens failed in 100 cycles or less, with tensile strength values ranging from 79.5 MPa to 322.6 MPa. The reason for this large experimental variability is attributed to the dispersion of imperfection sizes, with critical sizes ranging from 92 μm to 3443 μm, proving the importance of combining the information on the defect population with the assessed tensile strength.

1. Introduction

The experimental assessment of the mechanical strength of brittle and quasi-brittle materials is challenging and must deal with many critical issues, being the main ones: (i) the difficulty in obtaining uniaxial strength results, and (ii) the large variability of the measured strength for the same material.

The first issue is discussed at length in [1], whose focus is the development of the Ultrasonic Tensile (UST) test method and its validation on graphite R4550. This innovative methodology is employed in this paper to estimate the quasi-static tensile strength of alumina 99.5 %. Despite employing an ultrasonic testing device specifically developed for accelerated uniaxial fatigue tests investigating the Very High Cycle Fatigue (VHCF) life region, the UST test method was designed to induce specimen failure in a limited number of cycles (around 100) and to minimise the fatigue damage influence on the results. In particular, the specimen works in a resonance condition, designed to have the first longitudinal resonance frequency close to 20 kHz, with a geometry ensuring the strain required for failure.

Particularly, as pointed out in [1], the UST test method avoids or minimises the main issues that arise when traditional tensile tests for brittle materials are carried out, i.e., specimen failure near the mechanical grips of the testing machine in test configurations where clamping is required, and the necessity of a high precision alignment of the testing machine to avoid bending spurious stresses. Additionally, the UST test method does not require the estimation of the uniaxial strength from a multiaxial stress state, and allows testing of larger loaded volumes, i.e., the material volume subjected to stress close to the maximum stress. These limitations are frequently encountered in tests designed to avoid the use of mechanical grips and reduce alignment issues, e.g., three and four-point bending [2–4], ring-on-ring, ball-on-three-balls [5], ball-on-ring [6], Brazilian test [7,8], ring compression [9], ring-hoop tension [10,11].

Meanwhile, the second issue concerns the wide variability of experimentally assessed tensile strength data even for the same specimen geometry and testing configuration [12,13], mainly related to the presence of internal flaws. These flaws – such as pores, inclusions, and cracks – are unavoidably present, despite often being reduced, limited by optimised production processes, and are sources of stress concentration and possible origins of crack propagation [14,15], having a considerable influence on the variability of mechanical properties of brittle materials, characterised by low capacity of absorbing deformation energy, contrary to ductile materials [16]. Moreover, internal defects in brittle materials are particularly critical when submitted to normal stresses that cause crack opening, corresponding to mode I fracture according to Irwin's definition [17]. Therefore, an efficient method to predict the mechanical resistance of a brittle material component should rely on the knowledge of its intrinsic flaw population, i.e., the discontinuities that are potential weakest links in the material, as well as its global behaviour under uniaxial loads, which is the most influential factor for crack propagation.

A widely used method for assessing the influence of intrinsic flaws on

* Corresponding author.
E-mail address: ana.pagnoncelli@polito.it (A.P. Pagnoncelli).

https://doi.org/10.1016/j.matdes.2024.112680
Received 28 November 2023; Received in revised form 15 January 2024; Accepted 16 January 2024
Available online 24 January 2024

the mechanical strength of brittle materials is the statistical analysis of the experimental data conducted on multiple sets of specimens with different loaded volumes. This analysis employs largest extreme value distributions, such as Weibull [18] and Gumbel [12], to describe the experimental evidence that a larger material volume has a larger probability of containing a larger flaw, resulting in a lower global strength for that specimen. However, this statistical method, often referred to as scaling or size effect, requires experimental data on multiple sets of specimens, each set with a different loaded volume, considerably increasing the total number of samples to test, as well as having its effectiveness tied to how much the loaded volume can be increased throughout the sets.

As an alternative, many authors have been achieving the correlation between material strength and intrinsic flaws through the use of 3D x-ray imaging technology, whose application in the characterization of internal defects has seen a rapid increase in recent decades, frequently attributed to the diffusion of additive manufacturing methods, that usually require a more detailed defect analysis [19–21]. This method consists of conducting micro-Computed Tomography (micro-CT) scans on the specimens before the destructive test is conducted to assess the defect population within the loaded volume [22]. Through this procedure, internal defects can potentially be characterised according to their geometry – size, shape, spatial orientation –, distribution, quantity, and position within the specimen and relative to other defects. Additionally, this analysis can also provide evidence about the possible causes of the defects, for instance, inclusions caused by impurities amidst the raw components, poor bonding between raw components, pores that are often filled with gas, and internal cracks that could have propagated after sintering.

The present paper combines the UST method, recently developed by the Authors and comprised of the experimental and numerical procedures detailed in [1], with defect analysis through micro-CT inspection to characterise alumina 99.5 %. The applicability of the UST test method to obtain the tensile strength of a high-resistance ceramic material is verified within this activity. A method for defining the critical defect in each specimen is provided, as well as its size and position within the specimen. Meanwhile, the UST method, which estimates the normal stress distribution on the entire specimen at failure, provides both the maximum global stress applied to the material, as well as the local nominal stress applied on the critical defect, here referred to as ultimate tensile strength. These two experimentally measured quantities, i.e., ultimate tensile strength and critical defect size, are then correlated through an empirical formulation for the Stress Intensity Factor (SIF).

Therefore, the novelty of this work consists of three aspects: (i) the validation of the novel UST test method to estimate the quasi-static tensile strength of technical ceramics, specifically alumina 99.5 %, (ii) the development of an experimental procedure relying on micro-CT scanning to identify the critical manufacturing defect size of the specimens submitted through the UST test, and (iii) the correlation of the quasi-static tensile strength with the critical defect size through an empirical formulation to calculate stress intensity factors. By combining the UST test method with the internal defect analysis, a robust procedure for the characterization of brittle materials is provided, while its validation on alumina 99.5 % proves its reliable applicability to most technical ceramics used in different industrial fields, in particular medical and aerospace.

2. Material and specimen geometry

As mentioned in the Introduction, the material adopted in the experimental procedure is alumina 99.5 %, specifically rods, i.e., constant circular cross-section specimens, which, according to the chosen supplier, are produced through extrusion and sintering. Since the same testing equipment described in [1] is used in this work, which is briefly recalled in Subsection 4.1, the selection of the specimen length and diameter also follows the same requirements. Mainly, it should reach the first longitudinal natural frequency around 20 *kHz*, and it should guarantee a maximum stress capable of inducing tensile failure of the specimen within the ultrasonic testing machine amplitude output limit. The material parameters used to define the alumina specimen geometry follow the values provided by the supplier datasheet, presented in Table 1.

Table 1
Alumina properties considered for specimen design.

Design parameters	
Density $[kg/m^3]$	3900
Elastic modulus $[GPa]$	375
Poisson ratio	0.26
Strength, 3-point bending $[MPa]$	440
Strength, 4-point bending $[MPa]$	340

Since the machine can operate in a frequency range between 19.5 *kHz* and 20.5 *kHz*, the specimen length is calculated so that its natural frequency is 20.0 *kHz*. This way, the specimen resonance frequency is still likely to remain within the required range even in case of slight discrepancies in material properties (density and elastic modulus) from datasheet values. To demonstrate the design process, Fig. 1a shows the stress amplitude response on the specimen simulated in Ansys Workbench when a longitudinal harmonic displacement with amplitude 120 μm, resulting from the maximum machine output, is applied to one end of the specimen. In the simulation, solid hexagonal elements are used, the specimen has the first longitudinal mode natural frequency at 20010 *Hz*, and both of its ends are free.

Meanwhile, Fig. 1b shows the measurements of the final design. Since, in this case, the geometry of the cross-section does not affect longitudinal natural frequencies, it was selected as the largest diameter available, i.e., 10 *mm*, aiming to increase the loaded material volume. The simulation in Fig. 1a also shows that the maximum achievable stress of 577 *MPa* is higher than the strength provided by the supplier for 3-point bending tests. Since specimens subjected to bending tests are characterised by limited loaded volumes, reducing the likelihood of a large defect in the high-stress zone, it can be reasonably expected that the tensile strength in axial tests is smaller.

Once the actual specimens are obtained, a preliminary characterization is conducted to verify their proper compliance with the design parameters. This verification consists of measuring their dimensions and mass, and their natural frequency through the Impulse Excitation Technique (IET) [23]. Table 2 reports the properties calculated through those measurements for the 10 specimens considered in this work, showing that all three values are larger than those adopted in the initial design, but still within the expected values for alumina 99.5 %, while respecting the machine operating frequency range.

3. Defects characterization procedure

This section deals with the micro-CT inspections carried out in this study, providing details on the scanning parameters, and on the analysis process to characterise the specimen internal defects. Finally, the method for assessing the critical defect is detailed.

3.1. x-ray micro-computed tomography

In recent decades, the rapid advances in x-ray tomography for medical diagnostics have allowed its extension in the materials research field, in part thanks to its concurrency with the growth in additive manufacturing technology [24], pushing micro-CT scanning application as a non-destructive internal inspection method. These analyses provide not only information on the component defectiveness and reliability but are also used as the basis for process improvements and the final product quality control [19].

Taking advantage of these developments, this work utilises a cone-

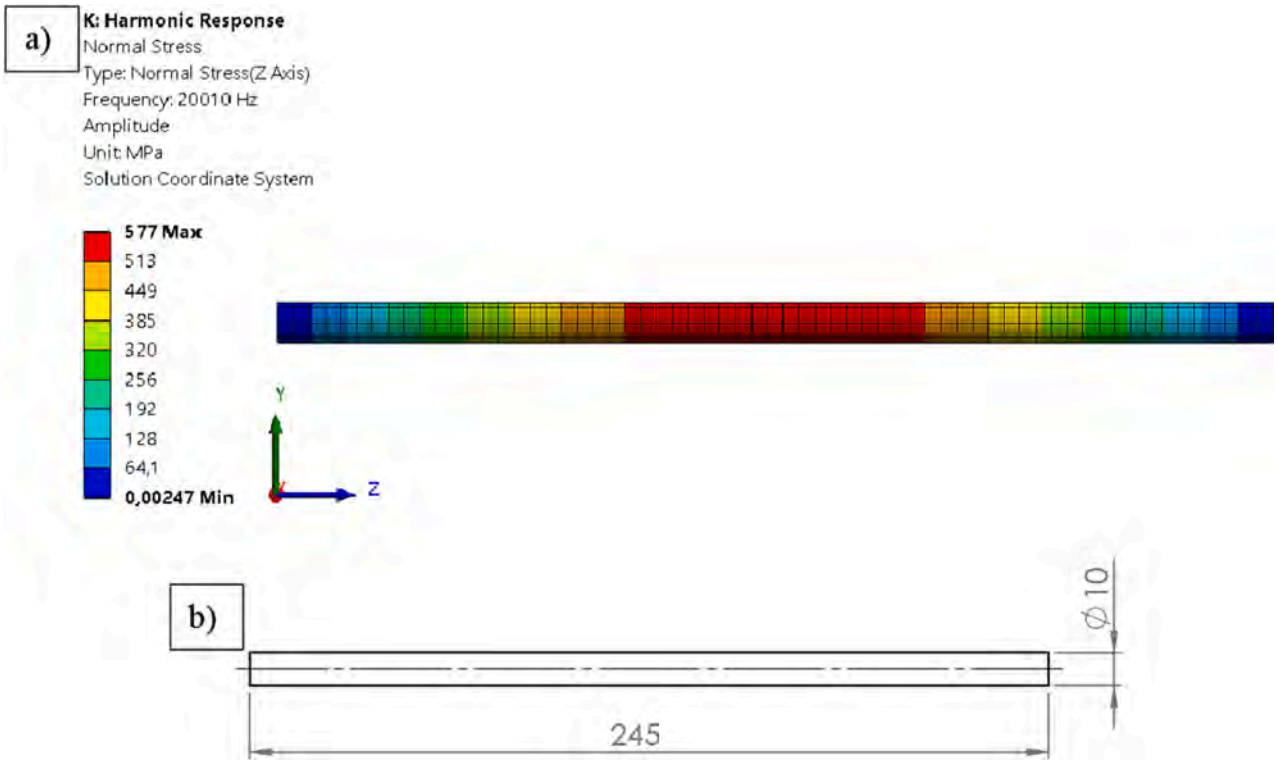

Fig. 1. (a) FEM calculated longitudinal stress for maximum machine output, and (b) specimen design (distances in [*mm*]).

Table 2
Preliminary characterization of alumina specimens.

Property	Mean	Standard deviation
Density [kg/m^3]	3968.8	1.3
Frequency [*Hz*]	20362	25
Elastic modulus [*GPa*]	395.1	0.9

beam micro-CT scanner designed and constructed by Fraunhofer IKTS. The machine consists of an x-ray source (or tube), a flat detector panel and a stage that holds the sample to be scanned, as shown in a top view schematic in Fig. 2a. It is important to underline in Fig. 2 that the coordinate system, with the z-axis coinciding with the vertical direction, will be the same adopted in all instances of this work, as its global coordinate system.

The stage and the detector can translate in the three axis directions, while the source remains fixed. The x-rays are generated inside the tube as ionising radiation, by passing a high voltage current through a tungsten filament, and take the form of a cone after exiting the source. Once the scan is started, the stage rotates around its vertical axis, z, as in Fig. 2, stopping in constant angle steps from 0° to 360° so that the specimen projections can be acquired.

The beam conic disposition allows magnifications up to a micrometrical scale, following the equation for the resolution:

$$r_{CT} = p_p \bullet \frac{SOD}{SDD} \tag{1}$$

being *SOD* and *SDD*, respectively the source-object distance and the source-detector distance, as described by Fig. 2a, and p_p the pixel pitch, i.e., the physical length of the side of each detector pixel. The maximum allowed value of *SDD* is 1900 *mm*, and a minimum *SOD* is 25 *mm*, requiring a minimum difference between *SDD* and *SOD* of 400 *mm*, to avoid collision between detector and stage. The detector has a pixel pitch $p_p = 200\ \mu m$, being comprised of 2048×2048 *pixels*. A full scan in this machine can contain up to 6400 projections. The maximum voltage of the x-ray source is 300 *kV*, and the maximum power 50 *W*, with the maximum resolution achievable by the tube being 3 μm.

3.2. 3D digital image reconstruction and defect analysis

Once all the projections are acquired, the software VGSTUDIO MAX 3.5 is used for digital image reconstruction and defect analysis. The raw projections from the micro-CT scanner are reconstructed using Feldkamp's algorithm [25] for cone-beam scanners, which converts the pixels from the projections into their 3D counterpart, called voxels. Each voxel is associated with a value in the grayscale, according to the beam intensity values captured by the detector during the projection acquisition.

After the reconstruction, the porosity/inclusion analysis module, with the algorithm VGDefX, is used to search for internal imperfections. The voxels with higher grayscale values are brighter and correspond to zones of high x-ray attenuation, whereas voxels with lower grayscale values are darker and represent lower attenuation regions. The algorithms for defect analysis use these values to identify material flaws, which are usually referred to either as porosities/voids – the darker spots, representing a lack of material – or as inclusions – the brighter spots, potentially containing a higher density constituent. The final report contains information such as size (volume, surface area, projected area on each of the three planes of the defined coordinate system, maximum diameter, equivalent diameter, and projected length on each cartesian axis), position according to the adopted coordinate system, and the composing voxels statistics (minimum, maximum, mean grey values and their deviation).

3.3. Scanning parameters and analysis criteria

Alumina is expected to be homogeneous, with its chemical components able to attenuate the x-rays in a way that generates good contrast in the results, with only mild x-ray filtering necessary. Particularly, a copper filter is adopted, as shown in Table 3 with the other test

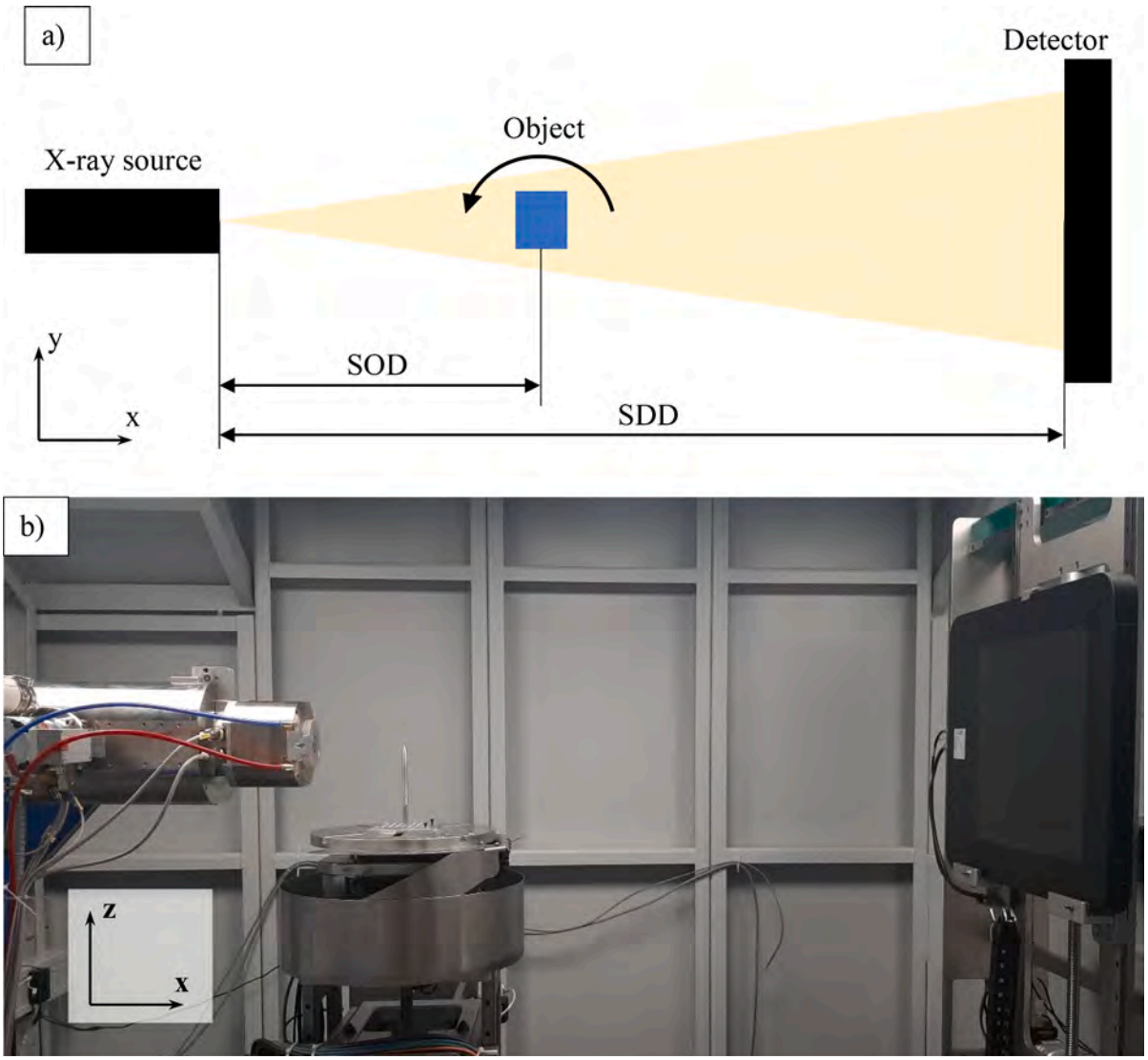

Fig. 2. (a) Schematic top representation of the cone-beam micro-CT scanner, and (b) its frontal picture.

Table 3
CT scanner configuration adopted for the alumina specimens.

Parameter	Set value
Tube current [μA]	80
Tube voltage [kV]	240
Exposure time [s]	1.0
SOD [mm]	55
SDD [mm]	1100
Filter	1.5 mm Cu
Number of projections	1600

parameters.

1600 projections are acquired, since, for this scanning setup, an increment of the projection number would not ensure a quality improvement. Furthermore, the configuration in Table 3 produces a resolution of 10 μm, which is enough to capture the full diameter of the specimen, and a portion of its length close to 18 mm in high quality.

However, as observed in Section 2, more specifically in Fig. 1a, these specimens have a large zone at their centre that could be considered as being at risk of fracture during the UST test. Therefore, to ensure that the zone where failure occurs is scanned beforehand, the micro-CT captured a span of at least 135 mm of the specimen centre, as illustrated in Fig. 3, which shows the final 3D reconstruction and its location on the specimen. To achieve this, each specimen was placed vertically on the stage and scanned 10 times, changing the stage z-position at constant steps accordingly. When all the reconstructions are positioned in VGSTUDIO, they generate the 3D representation in Fig. 3.

In Fig. 3, the darker rings in the 3D representation correspond to superposition zones that appear on two consecutive scanning steps. Since the cross-section is constant, each scanning step results in roughly the same geometry, i.e., a cylinder, hence the superposition zones are useful to verify the accurate positioning of each scan, by observing that unique features (e.g., a pore, an inclusion, a crack, a surface irregularity, etc.) from those zones are placed on the same global coordinate in VGSTUDIO.

With the scanned volumes properly positioned, the porosity/inclusion analysis module is used in two modes: void analysis, and inclusion analysis. The former looks for internal spots with an absence of material, such as pores and cracks, while the latter looks for zones with elements of larger density than the main material, such as agglomerates of impurities, referred to as inclusions.

For the analysed specimens, the results of interest should be the defect positions, computed for their respective geometrical centre, and the projected area on the xy-plane, corresponding to the specimen cross-section, according to the Murakami theory [26] for a 3D crack of

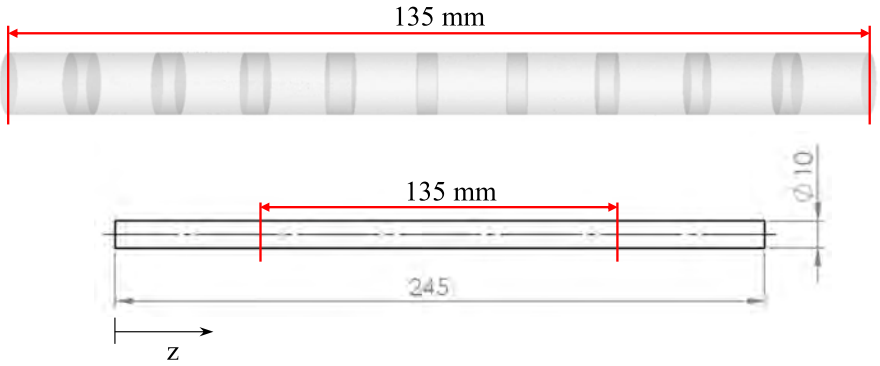

Fig. 3. Schematics of the scanned length of alumina specimens.

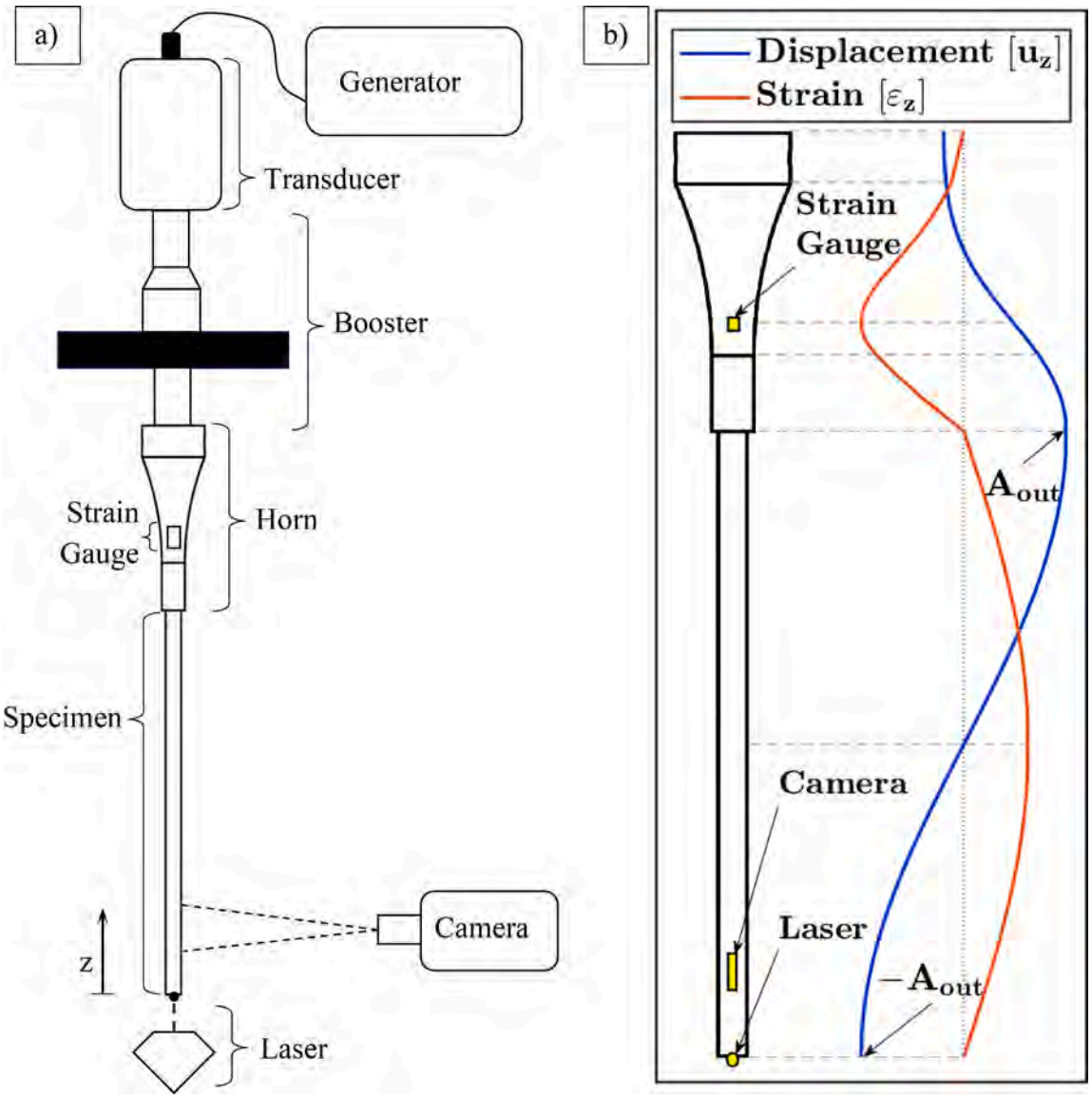

Fig. 4. (a) Configuration of the testing equipment for UST tests on alumina specimens, and (b) displacement amplitude and strain amplitude curves along the horn-specimen system.

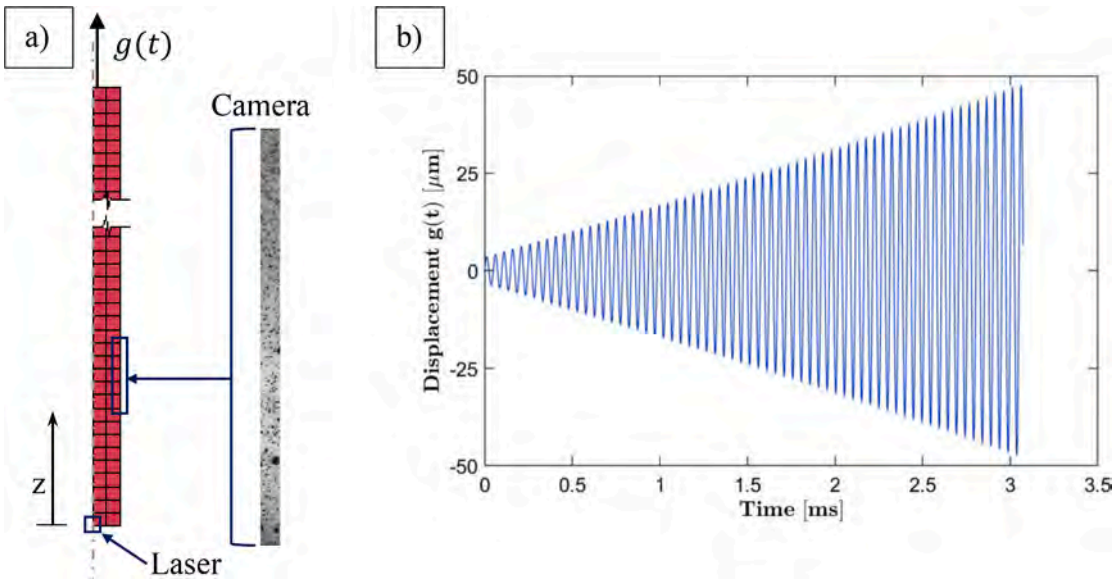

Fig. 5. (a) FEM setup schematics of the UST tests indicating the zones whose displacements are measured with the camera and the laser, and (b) boundary motion curve estimated for one of the specimens.

arbitrary shape. Since the UST test produces different local nominal stress along the specimen, as shown in Fig. 1a, the defect position is needed for analysis, while the defect size projected on the cross-section can be considered as the characteristic defect size also for the analysis of the quasi-static response, which is also in line with the definitions used by the models in [12] and [13], that use the square root of the area to define the defect size.

3.4. Critical defect identification

After the population of defects in the scanned volume is characterised, the UST test is conducted. Although carried out with a testing machine typically employed for fatigue tests (VHCF), the UST test is designed to replicate the failure conditions in a quasi-static tensile test and, as such, the fracture surface is not expected to show signs of crack propagation due to fatigue, as in fatigue tests on biomedical ceramics in [27]. Rather, the fracture surface of brittle materials tested through the UST test is expected to be the result of a catastrophic failure, which consists of almost instantaneous crack propagation, producing multiple small fragments of random sizes and shapes, most of which cannot be recuperated nor placed together to identify the crack propagation path and origin. For this reason, a relationship between the applied stress and the stress intensity factor cannot be directly obtained, but it can be indirectly obtained with the procedure developed in this paper.

Therefore, a different method to define the critical defect was devised, requiring the rescan of the specimen's broken pieces after the UST, specifically of its fracture surfaces and their vicinity. These scans are then reconstructed and overlapped with the scans collected before the UST, referred to as the original scan, allowing the identification of the defects that were originally present in the fracture zone, both those that were split by the fracture surface, and those contained in eventual missing fragments from the surface. Among these defects, the one with the largest projected area on the xy-plane will be selected as the critical defect with area A_c.

Since the accuracy of defect detection from micro-CT data can be influenced by several factors, e.g., the scanning parameters, the object geometry, the material, and the resolution, other studies in the literature compare results for porosity detection using microscopy, the Archimedes method, and micro-CT scanning [28–30]. According to these studies, it is reasonable to assume that internal defects from micro-CT data can be accurately identified if $\sqrt{A} \geq 4 \bullet r_{CT}$, with A being the projected area of the 3D flaw, and r_{CT} the scanning resolution as defined by Eq. (1) in Subsection 3.1. However, considering the scanning resolution, the relative error in the measurement of smaller defects is expected to be considerably larger.

Furthermore, experimental results in [28] indicate that micro-CT porosity analysis data can produce slightly different results for the same material sample but with different geometries, since the scanned geometry may increase or decrease the effect of phenomena such as x-ray beam hardening and scattering. Although, in the present work, a second scan on the same material with a different geometry, i.e., after the specimen is broken by the UST test and new fracture surfaces are generated, is carried out, the resulting differences are not expected to be enough to prevent a reliable overlap of the fracture surfaces over the original specimen to identify the critical defect.

4. Tensile behaviour characterization procedure

As described in [1], the UST test methodology is an experimental and numerical procedure that allows to characterise the behaviour of brittle materials, providing the material model and properties that are calculated through Finite Element (FE) optimization, aiming to reproduce the displacement curves experimentally acquired. In this section, a brief description of the UST test methodology is provided, focusing on the

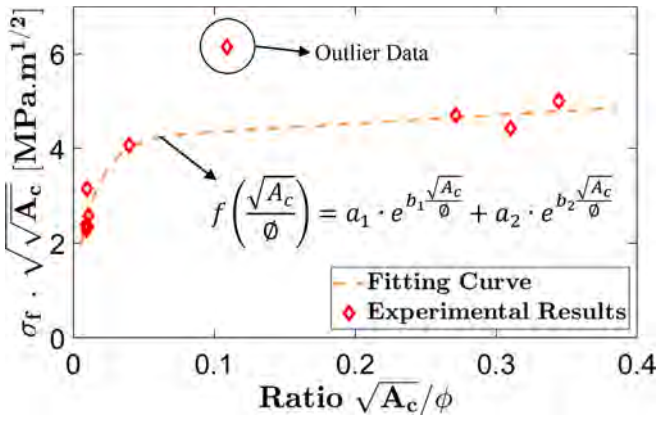

Fig. 6. Illustration of the fitting procedure to determine $f\left(\frac{\sqrt{A_c}}{\emptyset}\right)$.

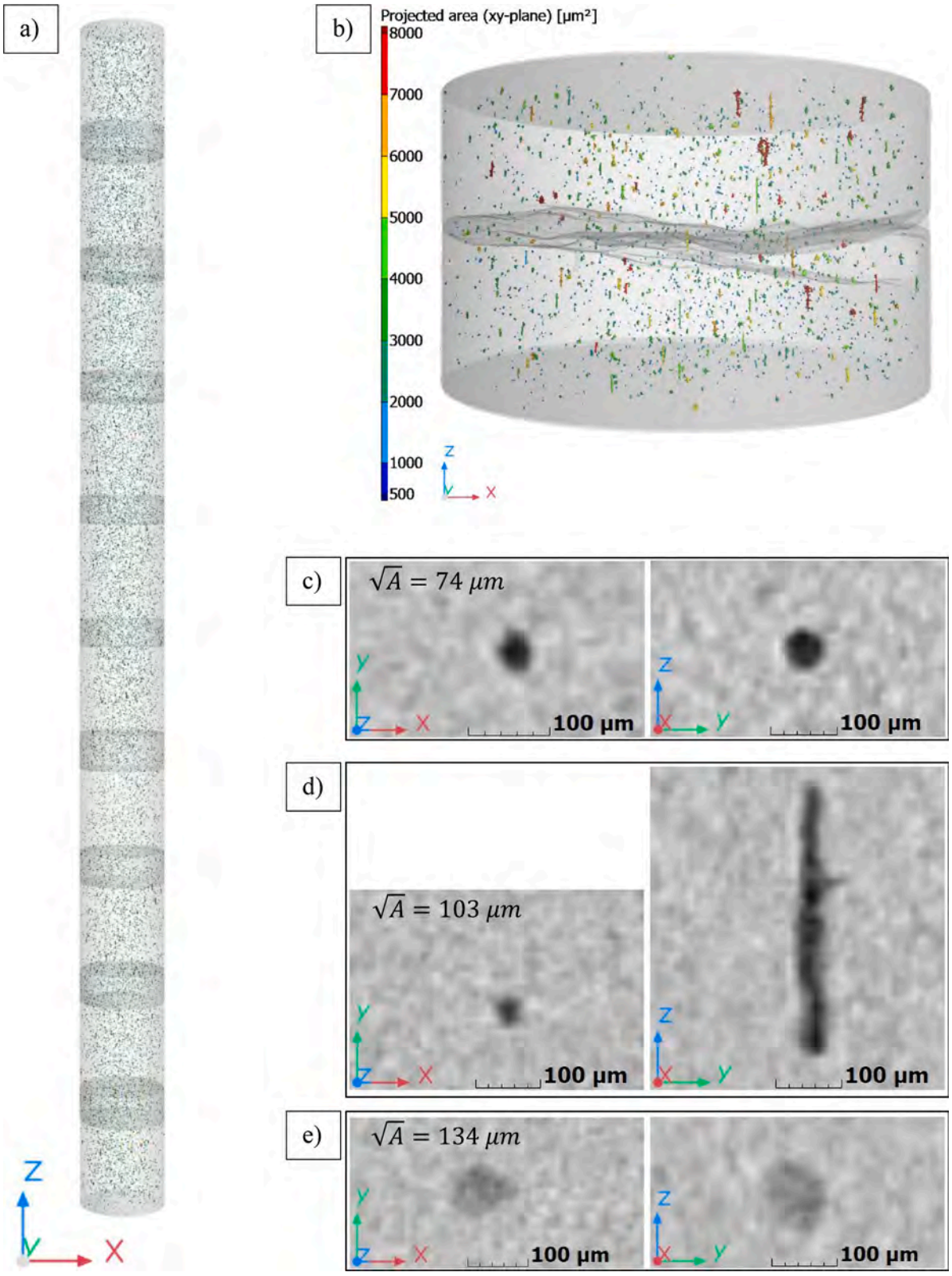

Fig. 7. Micro-CT data for alumina specimen 6, representing: (a) all the identified defects, (b) defects surrounding the fracture surface, (c) a highly spheric pore, (d) an elongated pore, and (e) a defect likely caused by poor bonding.

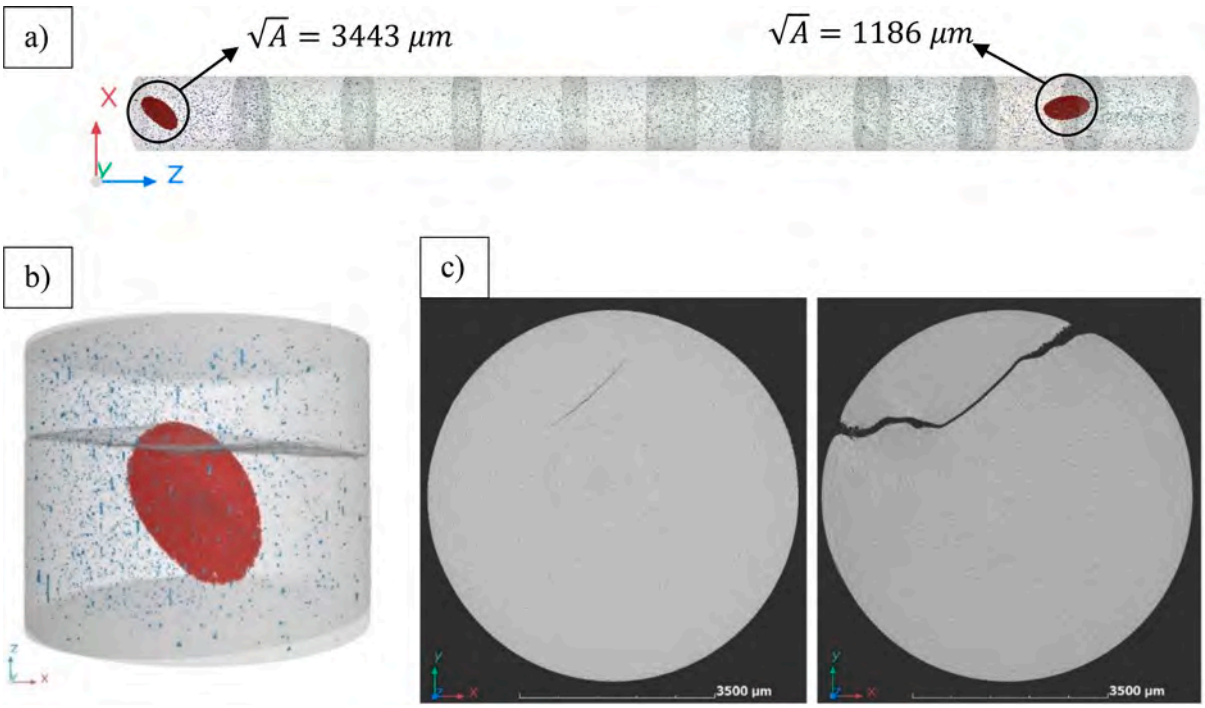

Fig. 8. Micro-CT data for alumina specimen 5, showing: (a) its two identified cracks with their respective sizes, (b) its fracture surface passing through the largest crack, and (c) the before and after of a fracture surface cross-section slice.

testing parameters adopted for the alumina specimens.

4.1. Experimental procedure

The ultrasonic testing machine, being the same as the one employed in [1], operates in a frequency range between 19.5 *kHz* and 20.5 *kHz*, and it is composed of an ultrasonic generator, a piezoelectric transducer, and a booster, all provided by Branson Ultrasonics, as shown in Fig. 4a. A horn, serving as a mechanical amplifier of the displacement generated by the piezoelectric transducer and the booster, is rigidly connected to the specimen with adhesive butt-joints, remaining free at the other extremity. Finally, three measuring devices are used during the test:

- an LK-G5001P laser from Keyence Corporation with a 392 *kHz* sampling rate.
- a FASTCAM SA5 1000 K-M1 high-speed camera from Photron with an acquisition rate of 420 *kfps* of size 24×512 *pixels*.
- Strain gauges measuring uniaxial strain on the horn at 2 *MHz* sampling rate.

Fig. 4b shows the analytically calculated longitudinal displacement and strain amplitudes along the horn and the specimen, considered linear-elastic, during regime resonance condition, with each curve normalised with respect to its maximum respective value. The graphics in Fig. 4b show that there are two displacement nodes, one within the horn length and one at the centre of the specimen.

Meanwhile, three strain nodes are present along the horn and the specimen length. In particular, a strain node is located at the horn-specimen interface, allowing the use of a common adhesive and avoiding fixture failures, one of the main issues when brittle materials are tested, as discussed in the Introduction. Additionally, since the other specimen end is free, the machine alignment is not a concern, provided that the specimen axis and the horn axis are properly aligned.

Moreover, the curves in Fig. 4b correspond to the instant of time when the harmonic vibration provided by the machine is at its peak, with the instantaneous displacement at the horn-specimen interface being equal to the output amplitude A_{out}. Despite this configuration of the ultrasonic testing equipment generating alternated tension and compression fields of the same magnitude on the specimen, alumina is expected to have a considerably larger resistance under compression, meaning that the specimen is guaranteed to break around a peak of tension, and the fracture surface is more likely to appear closer to the central cross-section, where larger strains are generated.

As indicated in Fig. 4b, the strain gauges are placed on the horn section characterised by the largest strain amplitude, measuring the machine output, and are used to calculate the displacement curve applied to the specimen, which is proportional to the strain curve, since the horn is designed to behave linear-elastically in the entire machine amplitude range. The laser is pointed at the centre of the specimen free extremity, detecting its vertical displacement. Meanwhile, the camera, contrary to the tests conducted on [1], is placed near the specimen free extremity, in the area indicated in Fig. 4b, acquiring a length of around 15 *mm* of the specimen. The camera frames are analysed with the Digital Image Correlation (DIC) technique, using the software DICe, specifically the tracking analysis mode, identifying the displacements along the longitudinal direction (z) from multiple points of the specimen lateral surface. Since the frame resolution is too small to allow a reliable analysis of strain through DIC, the camera is exclusively used for tracking displacements, which have smaller amplitudes near the specimen centre, thus justifying the decision to select a region with larger displacement amplitudes.

This equipment configuration allows the regime displacement amplitude at the horn-specimen interface to be in the range $13.2 - 120.0\ \mu m$. The ramp time is equal to 10 *ms*, amounting to around 200 cycles. The ramp is defined as the period between rest and regime conditions, i.e., between the start of the longitudinal vibration and the time necessary to reach the imposed amplitude. At the end of the ramp, the specimen should vibrate at constant amplitude, being in regime condition.

Since the goal of the UST test is to estimate the quasi-static tensile strength of the material, the selected regime amplitude should produce a stress that is larger than the material's expected tensile strength, therefore ensuring specimen failure during the ramp, since the UST test is designed to minimise the applied number of cycles and, consequently,

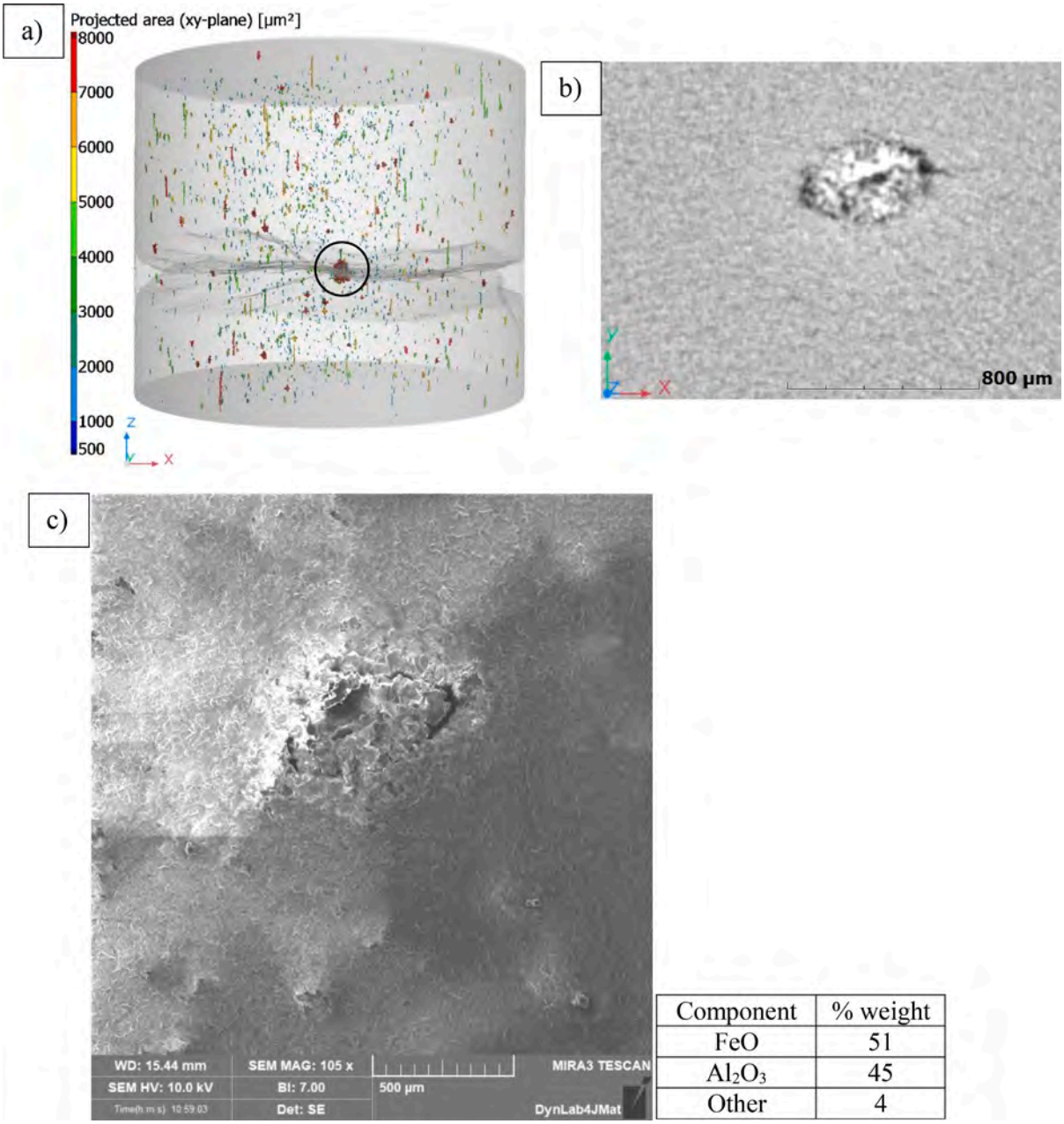

Component	% weight
FeO	51
Al_2O_3	45
Other	4

Fig. 9. Experimental analysis of alumina specimen 1: micro-CT scans containing (a) defects surrounding the fracture surface, and (b) slice of the inclusion, and (c) FESEM image with the EDS analysis results of the inclusion.

the influence of cyclic loading. Therefore, the machine output is set as 90 % of the maximum, i.e., during regime, $A_{out} = 108\ \mu m$, which, considering the values for density and elastic modulus experimentally calculated from the specimens, according to Table 2, in Section 2, should generate a maximum uniaxial stress of 547 *MPa*, considerably larger than the supplier datasheet values of strength for bending tests (Table 1, Section 2).

By respecting the above-mentioned conditions for the UST test, the specimen should break once the ultimate quasi-static strength is reached. Additionally, given alumina's brittle nature, failure is expected to propagate almost instantaneously and as soon as the crack originates, generating several ramifications and multiple smaller fragments of material, i.e., a catastrophic failure preventing the possibility of individuating the crack origin. Accordingly, a UST test for brittle materials may hardly provide a direct indication of the crack initiation stress, i.e., the stress in the vicinity of the critical defect. The experimental analyses have moreover proven that failures do not necessarily originate where the stress reaches its maximum, since defect location and defect size play a significant role in the crack initiation process. Indeed, failure origin is randomly distributed along the specimen length and within the cross-section. However, with the procedure developed and validated in the paper, the local stress at fracture surface position can be reliably

Table 4
UST test parameters for alumina.

Test Parameter	Value
Mean $f_{out}[Hz]$	20310
Standard deviation $f_{out}[Hz]$	41
Mean camera resolution $[\mu m]$	29.2
Standard deviation camera resolution $[\mu m]$	0.8
Regime $A_{out}[\mu m]$	108
Maximum stress at regime $[MPa]$	547

Table 5
Defect analysis results for each alumina specimen, comparing their respective critical and largest defects.

Specimen	Critical defect size [μm]	Critical defect type	Largest defect size [μm]	Largest defect type
1	397	Inclusion	The critical is also the largest.	
2	96	Pore	149	Pore
3	107	Pore	289	Pore
4	92	Pore	305	Pore
5	3443	Crack	The critical is also the largest.	
6	93	Pore	193	Pore
7	3102	Crack	The critical is also the largest.	
8	2714	Crack	The critical is also the largest.	
9	1089	Crack	1152	Crack
10	104	Pore	175	Pore

assessed by combining micro-CT analyses and finite element analyses of the specimens.

The remaining specific parameters for the UST tests on alumina are reported in Table 5. The selected output amplitude of 108 μm, and the indicated mean output frequency, considering a linear-elastic material model, using the measured values for density and elastic modulus, should achieve the mentioned stress level in the central cross-section in regime condition. The output frequencies for each specimen were defined by the horn signature procedure, in which the ultrasonic testing machine measures the horn-specimen system resonance frequency. Meanwhile, the camera resolution indicates the pixel size of the acquired images.

Once the collected data from the UST tests is synchronised, a preliminary analysis allows to count the number of cycles until failure, and to generate the displacement curves over time from the laser, the camera, and at the horn-specimen interface, which is estimated from the strain gauge measurements on the horn. The described experimental data are thereafter employed in the material model optimization described in Subsection 4.2.

4.2. Numerical procedure

The numerical procedure involves the simulation of the experimental test with the LS-DYNA software and the material properties optimization in LS-OPT, by applying the boundary conditions experimentally assessed. LS-DYNA was employed due to its capability of conducting dynamic explicit finite element analysis, where the nodal accelerations are solved directly, i.e., by multiplying the inverse of the diagonal mass matrix to the net nodal force vector, which is obtained by combining the contributions of external factors (boundary conditions, contacts, body forces, etc.) and internal factors (elemental stress, damping, viscosity, and hourglass control). Particularly, LS-DYNA allows the simulation of the UST test, which requires changing boundary conditions, corresponding to the application of a harmonic displacement with increasing amplitude at the horn-specimen interface, and could potentially entail the use of nonlinear material models that are often not present in other FE software, as observed in [1]. Meanwhile, the optimization process in LS-OPT serves the purpose of assessing the material properties that best fit the displacements measured by the laser and the camera, by varying the material properties values within the LS-DYNA solver at each iteration.

The specimen itself is modelled with shell elements, as shown in Fig. 5a, selecting the formulation for axisymmetric solid, volume-weighted with four integration points, resulting in 297 nodes and 196 elements. Meanwhile, the boundary condition, referred to as boundary motion curve in [1], represents the longitudinal displacement of the specimen section in contact with the horn, and assumes the form:

$$g(t) = \left(at^2 + bt + c\right) \bullet sin(2\pi \bullet f_{out} \bullet t) \tag{2}$$

being f_{out} the output frequency of the ultrasonic generator, t the time from the start of the test, and a, b and c empirical parameters obtained by fitting the strain gauges data, then converted into a displacement curve, shown Fig. 5b for one of the tested specimens. This fitting adapts to the measured frequency and ramp envelope, with the sinusoidal function eliminating measurement noise and avoiding numerical instabilities during the simulation.

Fig. 5a also indicates the approximate positions of the FE nodes that have the experimental displacements established as objectives for the material parameters optimization. Particularly, a camera frame from one of the specimens is presented as an example with a box comprising the 6 corresponding FE nodes on the specimen model, as well as the node at the centre of the free extremity of the specimen, in correspondence to the laser. For the optimization process, LS-OPT is set to minimize the values of the minimum square errors between the numerical and experimental displacements of the 6 nodes measured by the camera and the one measured by the laser, by changing the optimization variables corresponding to one or more material parameters, throughout the iterations.

The runtime of a single simulation in LS-DYNA increases with test duration and complexity of the adopted material model, while the optimization in LS-OPT has the additional influence caused by the number of variables being optimized. Indicatively, considering a linear-elastic material model for the tests in alumina conducted in this work, and the optimization of only one material property, i.e., the elastic modulus, the runtime for the single simulation is around 3 min, while each optimization run lasts around 1 h.

Once the material parameters are optimised, the validity of the optimization is verified through the calculation of the average determination coefficient for each specimen, defined as:

$$R^2 = 1 - \frac{\sum \left(u_{exp} - u_{num}\right)^2}{\sum \left(u_{exp} - \overline{u_{exp}}\right)^2} \tag{3}$$

being u_{exp} and u_{num} the experimental and the numerical displacements, respectively, at the corresponding FE node in the last 20 cycles preceding failure, which have the largest amplitudes, also defining the material strength.

With the FE model optimised and validated, the uniaxial stress calculated in each element is extracted, particularly the values for the highest global tensile stress achieved on that specimen, σ_{max}, and its ultimate tensile strength σ_f, which is the local nominal stress value extracted from the element in correspondence to the critical defect identified according to the procedure described in Subsection 3.4. By this definition, it is expected that $\sigma_{max} \geq \sigma_f$, since the element that achieves the highest tensile stress will not necessarily be the one originating failure, which could start in an element reaching a lower tensile stress but containing a larger defect.

The critical defect position within the specimen is also calculated through the analysis conducted in VGSTUDIO, being defined as the coordinates of its geometrical centre for the smaller critical defects. Although, realistically, crack propagation does not necessarily start at the centre of a defect, the loss of fragments during failure of brittle materials prevents the identification of its path, and, since most identified defects are considerably smaller than the finite element size, using the coordinates of its geometrical centre represents a good estimate. For the few cases in which the critical defect is larger than one finite element, it was verified that the z-coordinate of its centre coincided with an element located on the fracture surface, being adjusted accordingly when necessary.

5. Stress intensity factor formulation

With the successful completion of the steps described in Section 3 and Section 4, for each specimen, the ultimate strength σ_f and corresponding critical defect size A_c are obtained, allowing their correlation through a SIF formulation. When brittle materials are analysed, formulations for SIFs predominantly refer to Irwin's mode I loading [17], with the general definition for the SIF, K_I, in Eq. (4):

$$K_I = Y\sigma\sqrt{a} \tag{4}$$

being σ the stress in the crack opening direction, the tensile stress in this case, a the characteristic crack length, and Y a geometrical shape factor. For instance, Murakami [26] defines the SIF for the 3D problem of a crack with arbitrary shape in an infinite body as:

$$K_I = 0.5 \bullet \sigma \bullet \sqrt{\pi\sqrt{A}} \tag{5}$$

being A the area of the defect projected on the cross-section, perpendicular to both the crack opening direction and the stress σ. The main advantage of Eq. (5) is its applicability to randomly shaped material flaws through its definition of the characteristic defect size as $a = \sqrt{A}$. Although Murakami's definitions are more prominently used to calculate the SIFs from fatigue tests, the fact that Eq. (5) considers internal cracks in an infinite body should allow a proper estimate of the SIF of most defects identified in this work.

Furthermore, the shape factor Y introduces a flexibility to the calculation of K_I, in the sense that the same Y formulation could, within

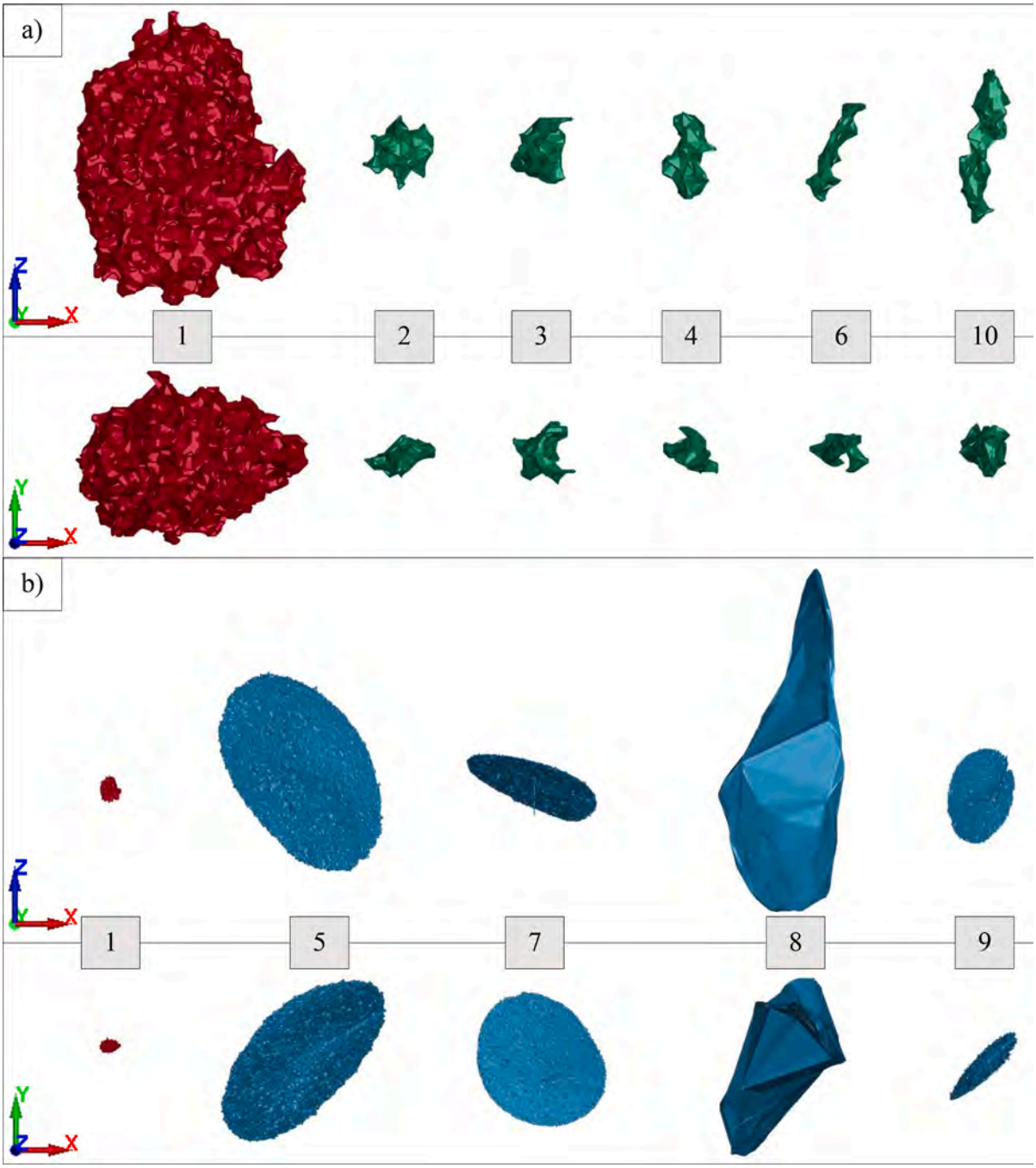

Fig. 10. Critical defects surface meshes, with frontal (xz-plane) and top (xy-plane) views, being: (a) inclusion in scale with the pores, and (b) inclusion in scale with the cracks.

the same material, take into consideration the behaviour of flaws with different shapes and sizes.

Following these definitions, A_c, representing the area of the critical defect projected on the cross-section, is used to calculate the stress intensity factors $K_{I,d}$ at failure for each tested specimen, defined according to Eq. (6):

$$K_{I,d} = \mathrm{C} \bullet \mathrm{Y} \bullet \sigma_f \sqrt{\sqrt{A_c}} \tag{6}$$

With Y calculated empirically through the data fitting of the experimental results for the entire set of specimens, as in Eq. (7):

$$\frac{1}{Y} = f\left(\frac{\sqrt{A_c}}{\varnothing}\right) = \sigma_f \sqrt{\sqrt{A_c}} \tag{7}$$

being $f\left(\frac{\sqrt{A_c}}{\varnothing}\right)$ a function of the critical defect size $\sqrt{A_c}$ and the specimen cross-section size $\varnothing$, corresponding to the diameter in circular cross-sections. The diameter $\varnothing$ is used as a geometrical correction, since the simple application of the defect size and the corresponding fracture strength implies a defect contained in an infinite body, being necessary to introduce a geometrical correction to account for the critical defects whose sizes are comparable to geometrical features. Indeed, the authors in [31] provide three different correction factors to calculate the SIFs of elliptical cracks embedded in cylindrical specimens subjected to fatigue tensile loads, which generally depend on the shape of the ellipse, its distance to the surface, and the specimen radius.

The UST is expected to minimise the fatigue damage, providing an estimate for the quasi-static tensile strength. The shape factor should be therefore carefully assessed for this specific case. For instance, in fatigue tests, surface defects are more critical than internal defects, as observed in [22], where the critical defect was generally found in proximity to the surface, even if larger defects were found within the material volume. Additionally, the expected absence of crack propagation signs on the fracture surfaces created by the UST test, as observed in [1], prevents the proper approximation of the critical defect shape to a regular elliptical shape, through the method demonstrated in [31].

Considering these observations, the only geometrical parameter used by [31] with a significant influence on tensile results, independently of the test being of fatigue or quasi-static, is the specimen radius. Hence, this work proposes a SIF formulation as a function of the ratio between defect size and specimen diameter $\frac{\sqrt{A_c}}{\varnothing}$, being able to include the cases in which the critical defect has a size that is too large for the hypothesis of infinite body to be valid.

The function used in the fitting of $f\left(\frac{\sqrt{A_c}}{\varnothing}\right)$ to the experimental data should have the simplest form capable of generating a good fit. Theoretically, if the infinite body hypothesis is valid, $\sigma_f \sqrt{\sqrt{A_c}}$ should be constant, since the material should fail once a fixed level of stress concentration is reached. However, as illustrated in Fig. 6 through the experimental results obtained in this work, there are critical defects with a ratio $\frac{\sqrt{A_c}}{\varnothing}$ above 30 %, causing a more complex distribution of $\sigma_f \sqrt{\sqrt{A_c}}$, which only could be fitted with a sum of exponentials.

Additionally, since this work opted for a simplified version of the geometrical correction factor through $\frac{\sqrt{A_c}}{\varnothing}$, the outlier datapoint, as indicated in Fig. 6, should be excluded from the fitting as its corresponding results are likely being more affected by other characteristics of this defect. Although these characteristics – such as shape, distance to other defects, distance to the specimen surface, etc. – are expected to have some level of influence on the SIF of all defects, they are also generally secondary to the effects of defect size relative to the specimen diameter. Therefore, defects that are not in agreement with this assumption should be properly excluded from the fitting.

As consequence of the fitting method, Eq. (7) results in $Y \bullet \sigma_f \sqrt{\sqrt{A_c}} = 1$. Therefore, to properly quantify a SIF value at failure, Murakami's formulation for 3D cracks with arbitrary shape in an infinite body [26] is used to estimate the constant C as the mean SIF of the critical defects that are applicable to Eq. (5):

$$C = \frac{0.5 \bullet \sqrt{\pi}}{n_k} \sum_{j=1}^{n_k} \sigma_{f,j} \sqrt{\sqrt{A_{c,j}}} \tag{8}$$

Therefore, Eq. (8) is only applicable to situations where the material body is infinite compared to the critical defect size, i.e., $\varnothing \gg \sqrt{A_c}$. Hence, the only specimens from the set whose stress intensity factors are considered in the calculation of the mean are those that respect this

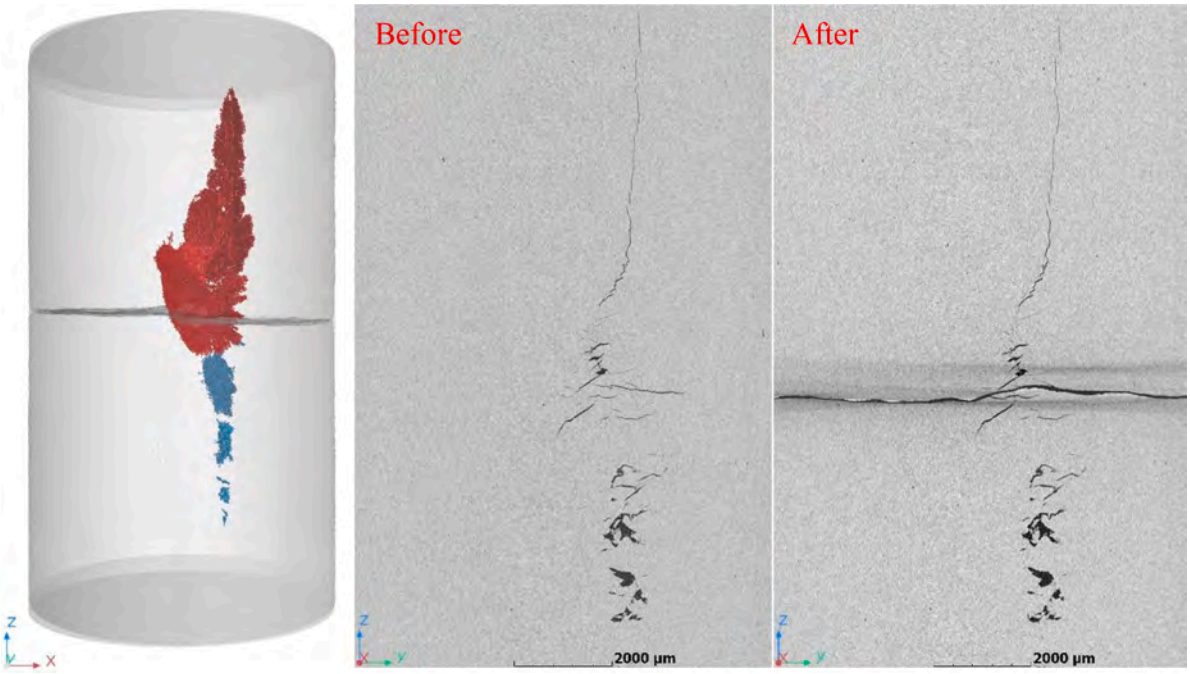

Fig. 11. Illustration of alumina specimen 8 cracks.

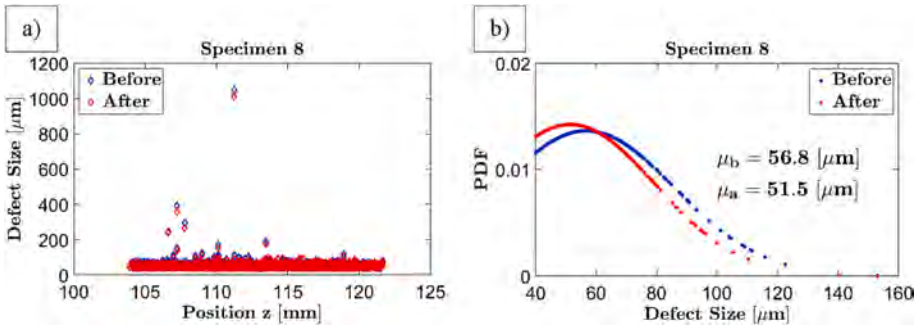

Fig. 12. Defect analyses before and after the ultrasonic test for alumina specimen 8: (a) defect sizes and their positions, and (b) their size normal PDF.

condition. With the empirical definition of C and Y, achieved through the analysis of the critical defects on each specimen as described, the stress intensity factors of the whole population of defects identified through the CT scans can be computed, only substituting $\sqrt{A_c}$ with the respective defect size $\sqrt{A}$, and σ_f with the nominal tensile stress σ at its respective position.

6. Results and discussions

Following the order of the sections presenting the methodology, this section is subdivided into: (i) defects characterization and critical defect identification, (ii) ultrasonic tensile test results with estimation of the ultimate strength, and (iii) stress intensity factor formulation and its application to the identified defects.

6.1. Defects characterization

The internal defects were classified into three groups: pores, cracks, and inclusion. Generally, alumina specimens are characterised by seemingly uniformly distributed pores, which account for almost the totality of identified defects. They tend to be small – being all under 350 μm in size ($\sqrt{A}$) – while their shapes indicate that they might be generated by the presence of trapped gas or poor fusion among the particles. 5 out of the 10 analysed specimens showed only pores in all their respective scanned volumes.

Fig. 7 shows the results of micro-CT scans for specimen 6, with Fig. 7a presenting the analysis of the complete scanned length and the absence of large defects, while Fig. 7b shows the defects surrounding the fracture surface after overlapping the tested specimen pieces with the original scan. Among all defects on the fracture surfaces and those split by them, the largest one is selected as the critical. Moreover, Fig. 7c – e compare the three observed types of pores, showing, respectively, a

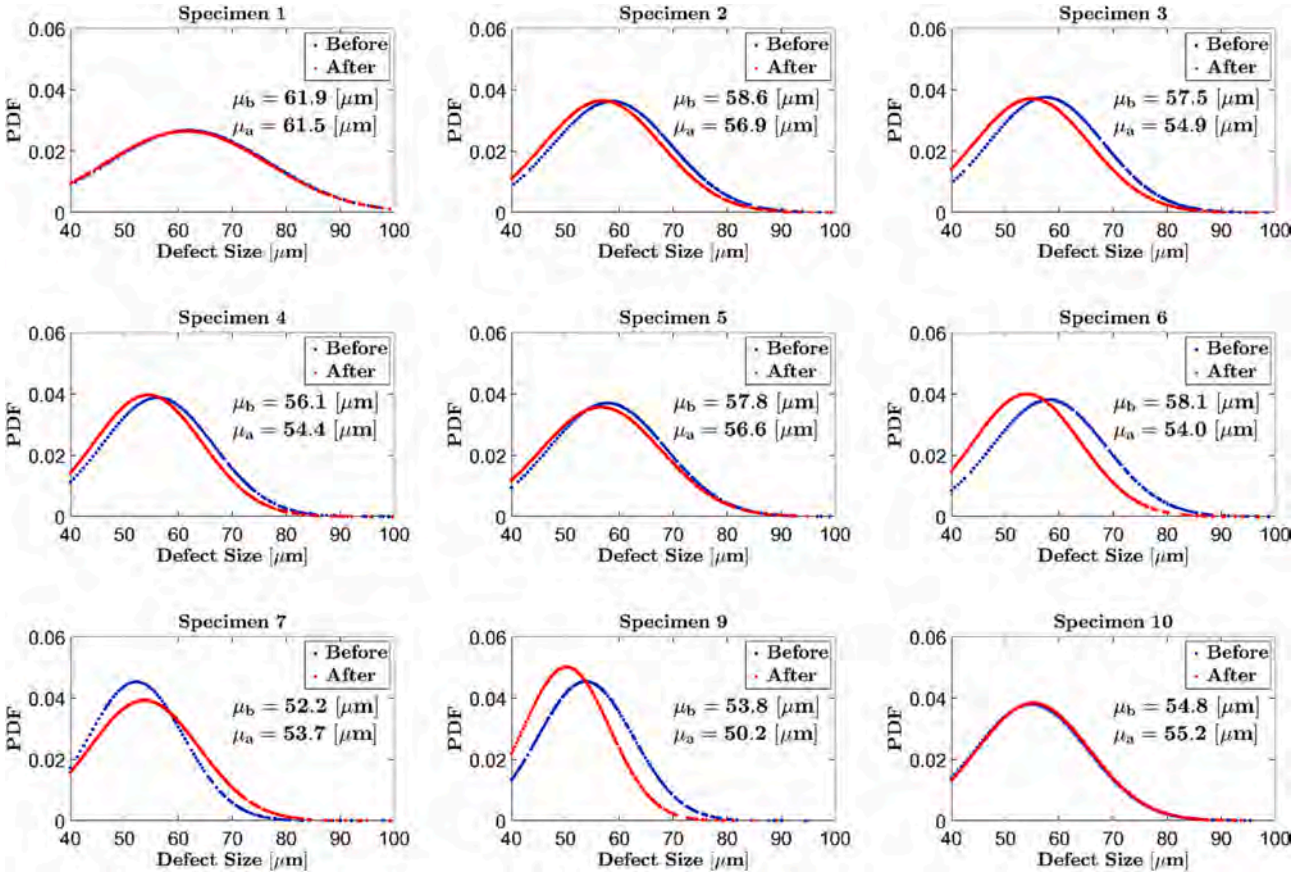

Fig. 13. Comparison of normal PDF of defect sizes before and after the ultrasonic test for the remaining specimens.

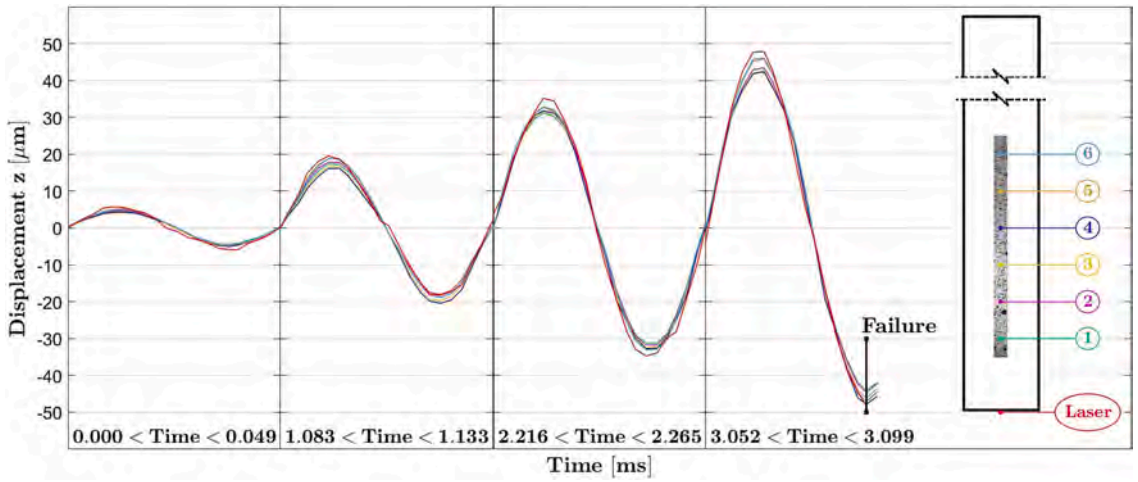

Fig. 14. Displacement results for specimen 6 showing the amplitudes at different time ranges up to failure.

defect with high sphericity, a defect elongated on the specimen axial direction (same as the rods extrusion direction before sintering), and a defect with irregular shape. While the first two are probably caused by gas, the latter might indicate poor bonding between particles, since some material seems to be present but in a smaller density than the surroundings, generating a zone with lower grey values, but still higher than that characteristic of complete voids, like in Fig. 7c and d.

In addition, multiple severe defects were detected in other specimens, albeit in much smaller numbers, in the form of cracks. These shapes are characterised by large sizes, often above 1 *mm*, and by their propagation through well-bonded material, which might indicate their appearance after sintering. 4 out of the 10 analysed specimens presented one or more crack-type imperfections, besides pores. One of these defects is shown in Fig. 8, (specimen number 5), with two cracks identified, with sizes 3443 μm and 1186 μm. The failure originates from the largest one, according to Fig. 8b, which shows the overlap between the destroyed specimen scans and the original. Meanwhile, Fig. 8c shows the comparison of the same slice taken before and after the ultrasonic test, confirming the crack being split during specimen failure.

Finally, observing the inclusion analysis results for all specimens, only one inclusion was found, being in specimen 1. Additionally, this specimen showed only pores, and no cracks, in the void analysis. Taking advantage of the fact that this inclusion was the critical defect, visible on the fracture surface, it was observed with a Field Emission Scanning Electron Microscope (FESEM). Moreover, an Energy-Dispersive x-ray Spectroscopy (EDS) analysis was carried out to identify the components present in the inclusion. Fig. 9 presents the defect analysis for specimen 1, with Fig. 9a showing the defects in the vicinity of the fracture surface, all pores, with the only inclusion highlighted. Fig. 9b contains the slice from the original scan, where the failure would split the inclusion. Meanwhile, the FESEM image in Fig. 9c, taken after the UST test, shows the inclusion on the fracture surface, along with the results from the EDS analysis of the inclusion, showing that it originated from an impurity of ferrous oxide II (FeO) mixed with alumina, while the 4 % of other elements are mostly carbon and oxygen.

According to the methods for the identification of the critical defect and its classification, Table 4 compares, for each specimen, the largest defect with the critical defect. Table 4 also indicates that the inclusion size is comparable with the largest pores, while the cracks are around 10 times larger. Additionally, since the UST test is designed to generate only uniaxial stresses, all specimens showed a tensile failure pattern, corresponding to Irwin's mode I, which is considered for the assessment of the SIF formulation, according to Section 5.

Table 4 also shows that specimens 2, 3, 4, 6, and 10, which contain exclusively pores in their defect populations, always present larger defects than the one identified as critical, which is expected. Since the uniaxial stress is not constant along the specimen length and, if no particularly severe imperfections are present even in lightly stressed regions, the critical defect will likely be in the higher stress zones, close to the specimen centre. Meanwhile, when a very large imperfection is present, the specimen could fail on a lower stress zone, as specimen number 5, shown in Fig. 8.

Given the variety of imperfections found within alumina specimens, concerning size, shape, and origin, a large scatter of ultimate strength is expected as well. To visually compare the critical defects, their surface mesh was extracted from VGSTUDIO and shown in Fig. 10, with Fig. 10a showing the inclusion, from specimen 1 (in red), in scale with the pores (in green), while Fig. 10b shows the inclusion in scale with the cracks (in blue). The defects view on the xy-plane corresponds to their respective projected areas, used to define $\sqrt{A}$. The defects in xy and in xz planes are shown.

According to Fig. 10, pores tend to assume one of the previously described shapes, even though their surfaces are often irregular. Meanwhile, the cracks are mostly penny-shaped, although not completely flat, being characterised by an elliptical form and often connected with neighbouring pores, increasing their irregularity and criticality. The only exception is specimen 8, which showed ramified cracks on the fracture surface and its surroundings, according to Fig. 11, showing the 3D overlap and the vertical slice of these cracks. The critical defect, this time in red, is apparently formed by multiple interconnected cracks, while the remaining represented imperfections are smaller cracks disconnected from the critical one. In Fig. 11, the pores are suppressed from the representation for better visualisation of the cracks.

Finally, a verification using defect analysis results was conducted to collect evidence that the small number of cycles necessary for reaching

Table 6
UST test experimental results for alumina.

Specimen	Maximum laser amplitude [μm]	Number of cycles	Test duration [ms]	Fracture surface position z [mm]
1	47.0	75	3.7	76.2
2	66.6	100	4.9	109.9
3	52.2	68	3.4	143.0
4	52.8	71	3.5	145.8
5	24.9	69	3.4	57.3
6	48.1	64	3.1	108.5
7	17.5	33	1.6	101.6
8	18.0	44	2.2	116.8
9	39.1	57	2.8	140.9
10	44.6	68	3.3	114.0

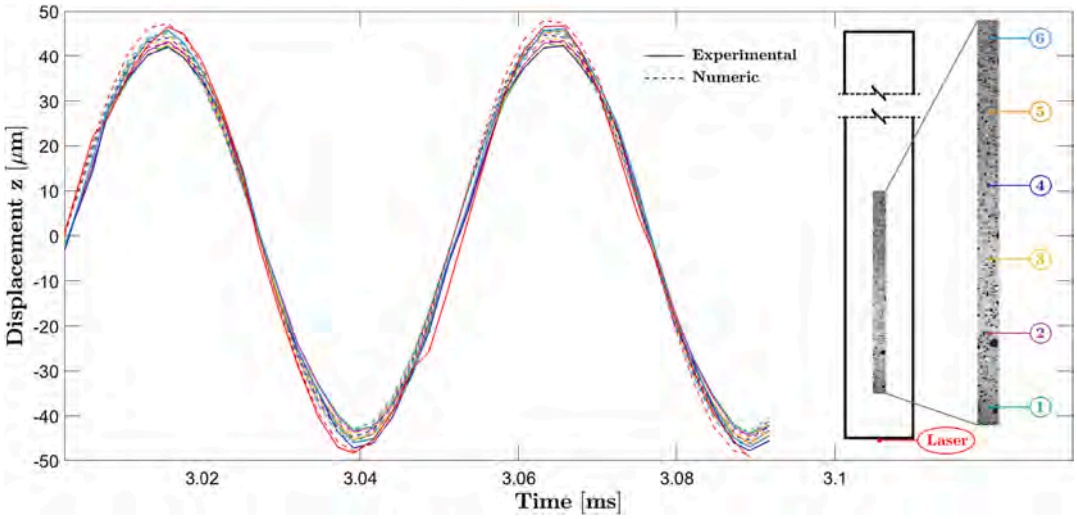

Fig. 15. Comparison between experimental displacement curves and those obtained through the numerical model for alumina (specimen 6).

the failure stress has not caused defect propagation as in fatigue tests. Since the micro-CT parameters used to scan the original specimens and their broken pieces were the same, the defect analysis results should also be approximately the same for the defects in the vicinity of the fracture surfaces, i.e., excluding defects that were split or went missing with eventual small fragments.

Therefore, a defect analysis with the same parameters as the originals was conducted on the post-UST scans, comparing the corresponding detected imperfections before and after the destructive test. The defects larger than 40 μm identified in both analyses were compared, as shown for specimen 8 in Fig. 12a, which plots the defect sizes with respect to their position from the specimen free extremity in the ultrasonic test. The estimated probability density function (PDF), by assuming that these defect sizes follow a normal distribution, is shown in Fig. 12b. Particularly, specimen 8, also having a large number of cracks, as seen in Fig. 11, that were not part of the fracture surface and were captured on the rescan, should provide more concrete evidence that the defects are not propagating due to fatigue. Indeed, the larger defects in the specimen have approximately the same sizes in both analyses, while the difference in mean size before (μ_b) and after (μ_a) the UST test is below the scanning resolution of 10 μm.

Although the scanning and analysis parameters were not changed, several other factors can influence the results, such as the newly created fracture surfaces whose irregular shapes cause localised beam hardening and scattering in the scans, as pointed out in Subsection 3.4. Moreover, there could be errors in the post-UST scans orientation over the original on VGSTUDIO, and effects of remaining substances, that are not present in the original scans, applied to the specimen lateral surfaces for the tensile test, e.g., the spray paint for DIC analysis, adhesives for eventual strain gauges and for attaching the specimen to the horn, all of which cannot be properly removed without causing additional damage to the fracture surfaces.

Nevertheless, the difference in the resulting mean defect size in all instances was seen to be below the scanning resolution, according to Fig. 13, showing the remaining specimens. Therefore, there is no evidence suggesting that defects have propagated due to the small number of cycles required to achieve the ultimate strength of each specimen.

Finally, observing the state of the fracture surfaces after the UST test, it was verified that all of them had fragments missing and no visible signs that would allow the identification of the defect where the crack initiated, such as those resulting from fatigue damage in ceramic materials analysed in [27]. This observation provides further evidence for the allegation of negligible fatigue damage, while corroborating the need for the proposed method for identifying the critical defect through the overlap of micro-CT scans before and after the destructive test.

6.2. Tensile behaviour characterization

Following the data analysis of each test, the displacement graphics for each specimen were obtained and plotted. Fig. 14 shows the results for specimen 6, measured with the laser displacement sensor, whose position is indicated on the specimen schematics, and the camera DIC for the 6 points in correspondence to the FEM nodes, as indicated in the recorded frame.

Fig. 14 shows the laser being in phase with the tracked points of the camera, as expected, and with failure occurring around a peak of tensile stress, i.e., where the measured displacements are near a valley, when, theoretically, the lower half of the specimen should have negative displacements and the upper half positive ones, as demonstrated by Fig. 4b. Moreover, it can be noticed that, even while ramping up to regime state, the displacement responses are symmetrical to the abscissa. Such verifications were conducted for all tested specimens, with the results reported in Table 6.

Table 6 shows the maximum displacement amplitude measured by the laser, with the camera measurements being close, since it records a zone close to the specimen free extremity, indicating the validity of the two measuring devices, being in agreement with the analytical displacement amplitudes shown in Fig. 4b. Moreover, the comparison between the amplitudes indicates that the testing machine is not able to reproduce the same ramp envelope throughout the different tests, particularly, specimens 3 and 5 sustained a similar number of cycles, with the latter achieving less than half the amplitude, indicating the necessity of using a different fit of Eq. (2) for each test. Nevertheless, the machine is capable of respecting the imposed ramp time, with all tests lasting less than 5 ms, while the theoretical regime amplitude measured by the laser should be 108 μm after 10 ms. Furthermore, the boundary motion curve defined in Subsection 4.2 was observed to properly respect these trends, especially since its general shape comes from strain gauge measurements on the horn.

Finally, Table 6 also reports the position in the z direction of the fracture surface, with $z = 0$ corresponding to the free extremity. The specimens that only showed pores as imperfections tend to fail closer to

Table 7
Alumina material properties.

Density [kg/m^3]	3969
Elastic modulus [GPa]	371.2

the specimen centre, located at $z = 124.5$ *mm*, i.e., at the higher stress zones, while those containing more severe flaws are largely dependent on their locations.

Observing the displacement curve trend in Fig. 14, it was established that the material model best able to simulate alumina 99.5 % is linear-elastic, given that the curves seemed to maintain themselves in phase with each other, as well as the symmetry with the abscissa as the movement amplitude increased. Therefore, the only material property that needs to be optimised in this model is the elastic modulus E. The experimentally assessed density, of 3969 kg/m^3, was considered. On the other hand, a Poisson ratio of 0.26 has been reasonably assumed.

To verify the successful optimization of the FEM, the displacements numerically obtained are compared to those experimentally measured, shown in Fig. 15 for specimen 6. It can be noticed in Fig. 15, through the observation of the last cycle before failure, that the linear-elastic material model applied to alumina is capable of reliably reproducing its behaviour during the ultrasonic tensile test. Additionally, the suitability of the linear-elastic material model to simulate the mechanical response of the tested alumina 99.5 % even in ultrasonic frequency rates agrees with literature data, which suggest a linear-elastic behaviour independently of the applied strain-rate [7,32].

Furthermore, the optimizations conducted in all specimens provide an elastic modulus of 371.2 *GPa*, which is 6.0 % smaller than the mean value measured through IET. However, this difference is expected, since experimental data from the literature suggests that, for brittle materials, the elastic modulus measured in dynamic non-destructive tests, such as IET, tends to be slightly larger than those measured in quasi-static tests, such as uniaxial compression, and three and four-point bending [23,33,34]. Although the UST test involves high strain-rates, it also generates strains on the specimen that are considerably larger than those caused by the impulse from an IET method, potentially causing the measured elastic modulus to show the same behaviour as in a quasi-static test. The final empirically obtained material properties can be seen in Table 7.

With the obtained material model, the results for each specimen could be extracted. Table 8 reports the determination coefficients, indicating the model's high accuracy for all specimens, the maximum amplitude achieved by the boundary motion curve, corresponding to the amplitude effectively applied to the specimen, the ultimate strength, corresponding to the one calculated on the critical defect, and its ratio to the maximum stress globally achieved on the specimen, defined as σ_f/σ_{max}.

Furthermore, Table 8 shows that, if a loaded volume for alumina 99.5 % were to be calculated based on this experimental dataset, it should correspond to the volume of material withstanding at least 68 % of the maximum stress, which is lower than the 90 % often adopted for fatigue tests, such as VHCF [35], representing further evidence to the already expected defect susceptibility of alumina. In this case, if the threshold for calculating the loaded volume were to be adopted as the lowest measured ratio σ_f/σ_{max}, then it would be $V = 9817$ mm^3, which is considered a large value when conducting size effect analyses [12,35].

According to the supplier, material strength data were obtained with 3-point bending tests according to the JIS R1601:2008 Standard [36], for 30 *mm* and 40 *mm* span between supports, both for rectangular cross-section specimens of 3 *mm* height and 4 *mm* width. The supplier results are compared to the results obtained in the UST test in Table 9, with the mean strength defined by the supplier as the specimen global ultimate strength, while the mean strength for the UST test corresponds to the local ultimate strength σ_f at the critical defect.

Given the statistical dependence between loaded volume and material strength, as detailed in the literature [12,13], it is expected that the supplier testing configuration will obtain considerably larger values for alumina strength. Indeed, Table 9 shows that the loaded volume in the UST test is over two orders of magnitude larger than either 3-point bending configuration.

Table 8
Results for each alumina specimen extracted from the optimised FEM model.

Specimen	Average R^2	Achieved $A_{out}[\mu m]$	$\sigma_f[MPa]$	σ_f/σ_{max}
1	0.997	49.7	203.8	0.85
2	0.997	66.4	322.6	0.99
3	0.997	53.4	248.6	0.95
4	0.997	54.1	249.0	0.94
5	0.994	26.0	85.3	0.68
6	0.996	48.5	236.4	0.99
7	0.986	16.8	79.5	0.97
8	0.981	18.4	90.2	1.00
9	0.996	39.4	186.1	0.96
10	0.993	47.2	232.6	1.00

Table 9
Comparison of strength data and loaded volumes for alumina in different test configurations.

Test configuration	Mean strength $[MPa]$	Loaded volume at $0.68 \bullet \sigma_{max}[mm^3]$
UST	193.4	9817
3-point bending, 40 mm span	340	14.2
3-point bending, 30 mm span	440	10.6

6.3. Stress intensity factors

Finally, according to Section 5, the critical defect size can be quantitatively correlated with the ultimate strength. As demonstrated by Fig. 6, which reports the experimental data for all the analysed alumina specimens, where $\sigma_f\sqrt{\sqrt{A_c}}$ is plotted in function of $\sqrt{A_c}/\varnothing$, with the diameter of the specimens $\varnothing = 10$ *mm*. The corresponding fitting curve is finally calculated as $f\left(\frac{\sqrt{A_c}}{\varnothing}\right) = 4.19 \bullet e^{0.387\bullet\frac{\sqrt{A_c}}{\varnothing}} - 3.12 \bullet e^{-65.1\bullet\frac{\sqrt{A_c}}{\varnothing}}$, while $C = 2.13$ $MPa \bullet m^{1/2}$. Therefore, the empirical formulation results in Eq. (9):

$$K_{I,d} = 2.13 \bullet \frac{1}{4.19 \bullet e^{0.387\bullet\frac{\sqrt{A_c}}{\varnothing}} - 3.12 \bullet e^{-65.1\bullet\frac{\sqrt{A_c}}{\varnothing}}} \bullet \sigma_f\sqrt{\sqrt{A_c}} \tag{9}$$

Fig. 16 shows the SIF values with respect to the critical defect size. The SIF values are close to the empirical equation, which behaves as a constant with the value of C regardless of the critical defect size.

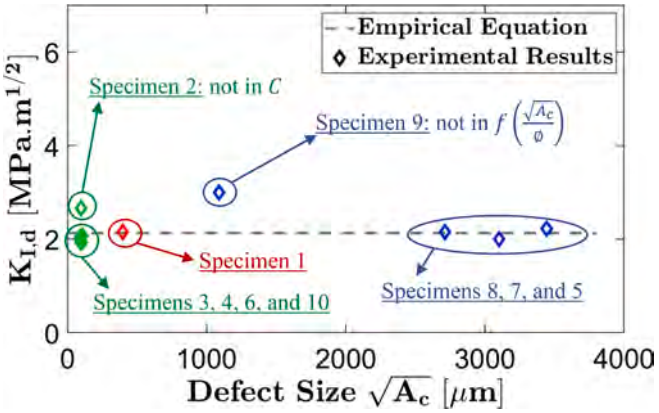

Fig. 16. Graphical representation of correlation between σ_f and $\sqrt{A_c}$ for alumina once the experimental data is applied to the empirical formulation for the SIFs, with the datapoints corresponding to the pores represented in green, the inclusion in red, and the cracks in blue. (For interpretation of the references to colour in this figure legend, the reader is referred to the web version of this article.)

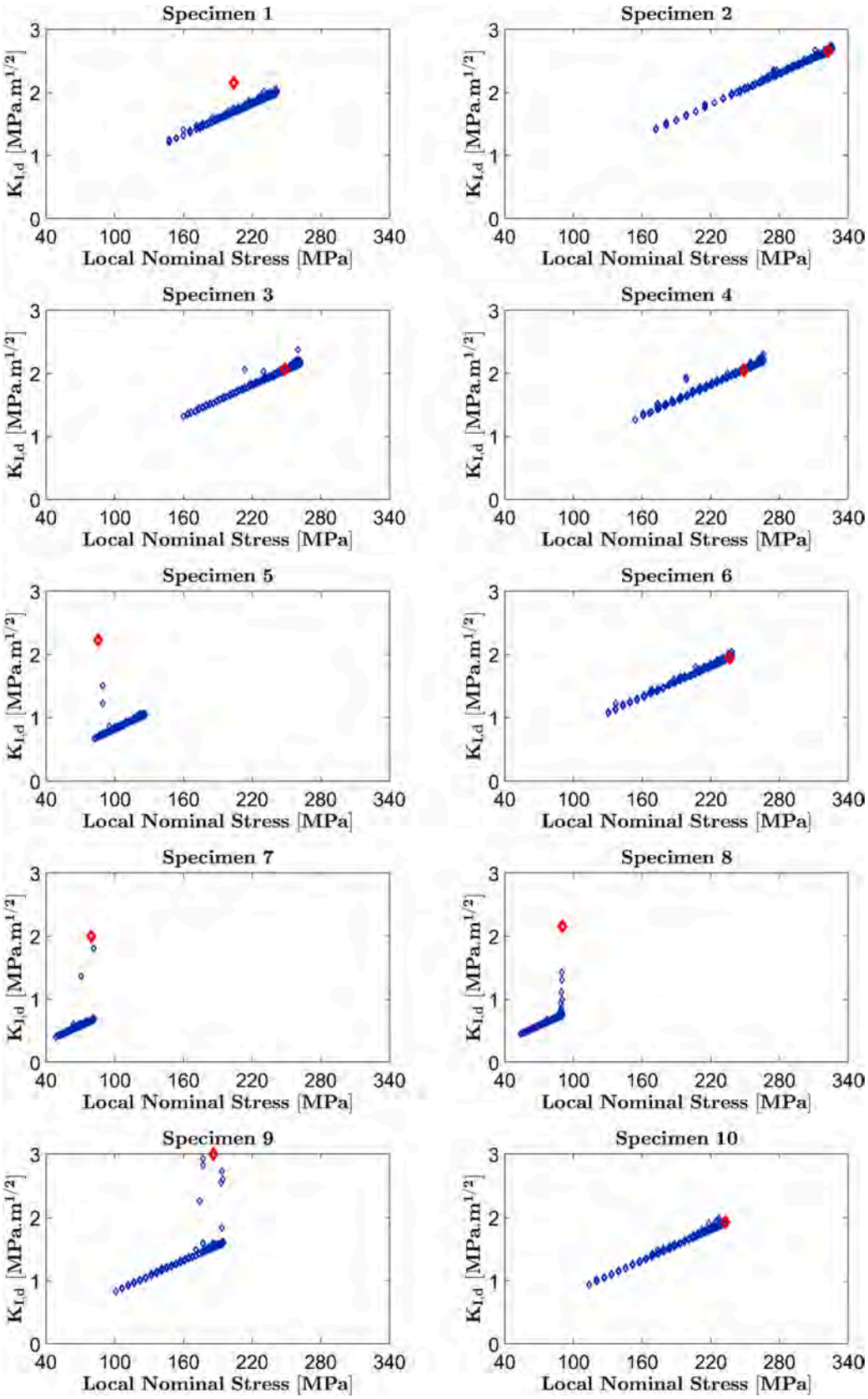

Fig. 17. SIF at failure on the 400 largest identified defects for each alumina specimen, with the respective datapoint corresponding to the critical defect highlighted in red. (For interpretation of the references to colour in this figure legend, the reader is referred to the web version of this article.)

Fig. 16 identifies which specimens are being represented by the datapoints using the same colour code as in Fig. 10, i.e., the pores indicated in green, the inclusion in red, and the cracks in blue. Particularly, the fitting of $f\left(\frac{\sqrt{A_c}}{\varnothing}\right)$ did not consider specimen 9, corresponding to the outlier datapoint indicated in Fig. 6, since its behaviour was outside the trend followed by the other specimens.

Additionally, only the pores were taken into consideration to calculate the constant C, since they are the only defects that respect the infinite body hypothesis, as pointed out in Section 5. However, specimen 2 was not considered to calculate C, since its value for $\sigma_f\sqrt{\sqrt{A_c}}$ was 25 % larger than the average for specimens 3, 4, 6 and 10. Since the size of the critical defects for these five specimens stays within the range $92-104\ \mu m$, the cause for this difference is the high value of ultimate strength reached by specimen 2, of 322.6 *MPa*, while the other four specimens stayed within the range 232.6 – 249.0 *MPa*.

Considering the whole set, Eq. (9) resulted in a mean SIF of 2.22 $MPa \bullet m^{1/2}$ with a standard deviation of 0.34 $MPa \bullet m^{1/2}$. The obtained values for $K_{I,d}$, although calculated using the values for the critical defect size, cannot be considered the critical SIF, or fracture toughness K_{Ic}, since they are obtained with an empirical formulation correlating nominal strength and critical defect size. Usually, experiments designed for the estimation of K_{Ic} rely on controlled cracks introduced in the specimen, with known geometry, defined position and direction for crack propagation, as indicated by the International Standard [37], and observed in the experiments conducted by [38] and [39]. However, all material imperfections identified in the present work, including the critical defects, are unintentionally created during the manufacturing process, being characterised by their randomness of shape, size, position, and orientation, therefore, not allowing the estimation of fracture toughness (K_{Ic}) values, according to the definition provided in International Standards, due to the unpredictability of the crack front location, crack propagation direction and the irregular morphology of the defects originating the fatigue failure.

As a further comparison, the empirical formulation in Eq. (9) was applied to the 400 largest defects identified on each specimen, to calculate the SIF generated by the nominal tensile stress being produced at each defect position when the failure occurred. The graphics in Fig. 17 show the obtained results, with each specimen's critical defect plotted in red.

Particularly, this analysis is to verify that the largest value of $K_{I,d}$ in the respective specimen was also caused by its critical defect, potentially validating Eq. (9). This does seem to be the case for all the specimens containing cracks (5, 7, 8, and 9), and for the specimen containing the inclusion (1). However, for the specimens that only presented pores (2, 3, 4, 6, and 10), although the value for the critical defect is generally among the highest, some cases, specifically specimens 3 and 4, showed SIF values up to 14 % larger than the ones associated with their respective critical defects, which could cast doubt on the validity of Eq. (9), indicating the influence of factors other than the size, such as shape, distance to the specimen surface, and distribution within the material, which could cause two smaller defects close to each other to be more critical than if just one slightly larger defect were in that same place.

Nevertheless, the formulation accurately predicts failure when severe defects are involved, which correspond to the most critical cases, where the strength levels are the lowest, while also providing a sufficiently good approximation in their absence. Therefore, it can still be applied to component design while also maintaining its simplicity, since it depends only on defect size and material dimension.

7. Conclusions

This research successfully achieved its three main goals, comprised of: (i) validating the innovative experimental–numerical procedure relying on the Ultrasonic Tensile (UST) test developed recently by the Authors to obtain the mechanical properties of a high-resistance ceramic, i.e., alumina 99.5 %, (ii) analysing the manufacturing defect population of the tested specimens and providing a method for defining the critical defect independently of the fracture surface conditions, and (iii) proposing a Stress Intensity Factor (SIF) formulation to correlate the critical defect size with the ultimate nominal tensile stress of each specimen.

The working principle of the UST test prevents the main issues typical of experimental tests on brittle materials, i.e., the possibility of failures at the interface with mechanical grips, and the introduction of spurious bending stresses caused by machine misalignments. Meanwhile, the induced uniaxial stress field eliminated the need for indirect estimation of the tensile strength from a multiaxial stress state. Finally, the ultrasonic device allowed testing of a high-resistance brittle material with a considerably larger loaded volume than those found in the literature.

The UST methodology was successfully applied to test alumina 99.5 %, with the subsequent estimation of the mechanical properties through finite element (FE) modelling and an optimization procedure. The choice of linear-elastic material for the FE model of alumina 99.5 % was proven accurate, with the optimization resulting in an elastic modulus of 371.2 *GPa*.

The internal defect analysis carried out with micro-Computed Tomography (micro-CT) allowed the characterization of the flaw population and the identification of the critical defect. The critical defects of the five specimens that only contained pores had sizes in the range $92-104\ \mu m$, the inclusion was the critical defect of its corresponding specimen, measuring 397 μm, the remaining four specimens had cracks as critical defects, with sizes in the range $1089-3443\ \mu m$. The large overall range of internal defect sizes affected the UST results, with the estimated ultimate strength values ranging from 79.5 to 322.6 *MPa*. Particularly, this fracture strength is smaller than that provided by the supplier. Nevertheless, the significantly larger loaded volume can explain this difference, since size effect significantly affects the mechanical properties of brittle materials.

The possible influence of fatigue damage introduced with the UST has been verified and excluded, indicating that the obtained strength results are a good representation of the quasi-static tensile strength of the tested alumina 99.5 %. Indeed, the number of cycles before specimen failure was limited (within 100), with a large portion at a small amplitude, being less likely to cause fatigue damage. Moreover, evidence of crack propagation of the non-critical flaws was not found when comparing the micro-CT scans before and after the UST test.

Finally, the critical defect sizes were correlated to the ultimate strengths, with the definition of an empirical SIF formulation for the tested alumina 99.5 %. The SIF has been computed for the largest defects identified on each specimen, with the critical defect always generating a SIF value amongst the largest values achieved on that specimen, thus validating the proposed formulation.

CRediT authorship contribution statement

A.P. Pagnoncelli: Conceptualization, Data curation, Formal analysis, Investigation, Methodology, Software, Validation, Visualization, Writing – original draft, Writing – review & editing. **A. Tridello:** Conceptualization, Resources, Supervision, Writing – review & editing. **D.S. Paolino:** Conceptualization, Resources, Supervision, Writing – review & editing. **L. Peroni:** Conceptualization, Methodology, Resources, Supervision, Writing – review & editing.

Declaration of competing interest

The authors declare that they have no known competing financial interests or personal relationships that could have appeared to influence the work reported in this paper.

Data availability

Data will be made available on request.

Acknowledgements

The research used the equipment of J-Tech and DYNLab Laboratory at Politecnico di Torino, co-funded by POR FESR Piemonte 2014-2020.

References

[1] A.P. Pagnoncelli, D.S. Paolino, L. Peroni, A. Tridello, Innovative tensile test for brittle materials: Validation on graphite R4550, Int. J. Mech. Sci. (2023), https://doi.org/10.1016/j.ijmecsci.2023.108679.
[2] M. Staudacher, T. Lube, J. Schlacher, P. Supancic, Comparison of biaxial strength measured with the Ball-on-Three-Balls- and the Ring-on-Ring-test, Open Ceram. 6 (2021), https://doi.org/10.1016/j.oceram.2021.100101.
[3] Y. Li, C. Zhong, T. Qin, M. Wang, Preparation and performance of CaO-MgO-SiO2-Al2O3-CaF2 glass/Al2O3 ceramic with high flexural strength, J. Non. Cryst. Solids 602 (2023), https://doi.org/10.1016/j.jnoncrysol.2022.122088.
[4] J.W. Fu, H. Haeri, V. Sarfarazi, M.F. Marji, Modeling the Ligament Breakage Mechanism in Concrete Specimens Using a Four-Point Bending Test, Strength Mater. 54 (4) (2022) 671–680, https://doi.org/10.1007/s11223-022-00445-9.
[5] J. Schlacher *et al.*, "Strength of additive manufactured alumina," *J. Eur. Ceram. Soc.*, vol. 40, no. 14, 2020, doi: 10.1016/j.jeurceramsoc.2020.03.073.
[6] M. Staudacher, P. Supancic, T. Lube, The Ball-on-Ring-test: Enhancing an analytical solution by numerical analysis for elastic deformation and small displacements, J. Eur. Ceram. Soc. (2023), https://doi.org/10.1016/j.jeurceramsoc.2023.06.016.
[7] J. Zheng, H. Li, J.D. Hogan, Strain-rate-dependent tensile response of an alumina ceramic: Experiments and modeling, Int. J. Impact Eng. 173 (2023), https://doi.org/10.1016/j.ijimpeng.2022.104487.
[8] Y. Zhou, J.W. Fu, D.C. Wang, H. Haeri, L.J. Sun, C.L. Guo, Numerical Investigation of the Influence of Circular Fillings on the Failure Mechanism in Samples Containing Nonpersistent Joints Under Shear Loading Conditions, Strength Mater. 54 (5) (2022) 880–888, https://doi.org/10.1007/s11223-022-00465-5.
[9] X. Zhang, Y. Yi, H. Zhu, G. Liu, L. Sun, L. Shi, Measurement of tensile strength of nuclear graphite based on ring compression test, J. Nucl. Mater. 511 (2018) 134–140, https://doi.org/10.1016/j.jnucmat.2018.09.010.
[10] J. Calaf-Chica, J. Martínez-Peña, P. M. Bravo Díez, and M. Preciado Calzada, "Ring Hoop Tension Test for yield strength estimation: Numerical analysis for a novel correlation method and applicability for mechanical testing of tubes and pipes," *Mech. Mater.*, vol. 169, 2022, doi: 10.1016/j.mechmat.2022.104295.
[11] J.W. Fu, V. Sarfarazi, A.A. Naderi, H. Haeri, M.F. Marji, T. Li, Calibrating a New Compressive-to-Tensile Load-Transferring Device for Determining the Direct Tensile Strength of Granite, Strength Mater. 54 (5) (2022) 959–966, https://doi.org/10.1007/s11223-022-00471-7.
[12] A.P. Pagnoncelli, A. Tridello, D.S. Paolino, Modelling size effects for static strength of brittle materials, Mater. Des. 195 (Oct. 2020), https://doi.org/10.1016/j.matdes.2020.109052.
[13] A.P. Pagnoncelli, A. Tridello, D.S. Paolino, Static strength of brittle materials under multiaxial nonuniform stress states: A novel statistical model for assessing size effects, Fatigue Fract. Eng. Mater. Struct. 44 (4) (Apr. 2021) 997–1013, https://doi.org/10.1111/ffe.13409.
[14] J.W. Fu, T. Li, H. Haeri, Acoustic Emission Monitoring of Crack Growth from Echelon Notches Using Numerical Simulation, Strength Mater. 55 (2023).
[15] Q. Wang, L.J. Sun, D.C. Wang, J.W. Fu, C.L. Guo, H. Haeri, Particle Flow Modeling for the Crack Growth Analysis of Non-Persistent Cracks, Strength Mater. 55 (2) (2023) 371–383, https://doi.org/10.1007/s11223-023-00531-6.
[16] A. Ghamari, H. Haeri, A. Johari Naeimi, Z. Najmi, V. Sarfarazi, Behavior of double K-BRB braces under lateral loading, J. Cent. South Univ. 28 (8) (2021) 2394–2406, https://doi.org/10.1007/s11771-021-4668-z.
[17] G.R. Irwin, Analysis of stresses and strains near the end of a crack traversing a plate, J. Appl. Mech. 24 (3) (1957) 361–364, https://doi.org/10.1115/1.4011547.
[18] W.S. Lei, G. Qian, Z. Yu, F. Berto, Statistical size scaling of compressive strength of quasi-brittle materials incorporating specimen length-to-diameter ratio effect, Theor. Appl. Fract. Mech. 104 (2019), https://doi.org/10.1016/j.tafmec.2019.102345.
[19] E. Maire, P.J. Withers, Quantitative X-ray tomography, Int. Mater. Rev. 59 (1) (2014) 1–43, https://doi.org/10.1179/1743280413Y.0000000023.
[20] J. Elambasseril, et al., 3D characterization of defects in deep-powder-bed manufactured Ti–6Al–4V and their influence on tensile properties, Mater. Sci. Eng. A 761 (2019), https://doi.org/10.1016/j.msea.2019.138031.
[21] S. Romano, A. Abel, J. Gumpinger, A.D. Brandão, S. Beretta, Quality control of AlSi10Mg produced by SLM: Metallography versus CT scans for critical defect size assessment, Addit. Manuf. 28 (2019) 394–405, https://doi.org/10.1016/j.addma.2019.05.017.
[22] C. Colombo, et al., Efficient experimental methods for rapid fatigue life estimation of additive manufactured elements, Int. J. Fatigue 167 (2023) 107345, https://doi.org/10.1016/J.IJFATIGUE.2022.107345.
[23] G. Nie, Y. Bao, D. Wan, Y. Tian, Measurement of the high temperature elastic modulus of alumina ceramics by different testing methods, Key Eng. Mater. 768 (2018), https://doi.org/10.4028/www.scientific.net/KEM.768.24.
[24] A. du Plessis, I. Yadroitsava, I. Yadroitsev, Effects of defects on mechanical properties in metal additive manufacturing: A review focusing on X-ray tomography insights, Mater. Des. 187 (2020), https://doi.org/10.1016/j.matdes.2019.108385.
[25] L.A. Feldkamp, L.C. Davis, J.W. Kress, Practical cone-beam algorithm, J. Opt. Soc. Am. 1 (6) (1984) 612–619.
[26] Y. Murakami, Theory of Elasticity and Stress Concentration. (2016), https://doi.org/10.1002/9781119274063.
[27] L.F. Valandro, A.C. Cadore-rodrigues, K.S. Dapieve, V. Machry, G. Kalil, R. Pereira, A brief review on fatigue test of ceramic and some related matters in Dentistry, J. Mech. Behav. Biomed. Mater. 138 (2023), https://doi.org/10.1016/j.jmbbm.2022.105607.
[28] W.W. Wits, S. Carmignato, F. Zanini, T.H.J. Vaneker, Porosity testing methods for the quality assessment of selective laser melted parts, CIRP Ann. - Manuf. Technol. 65 (1) (2016) 201–204, https://doi.org/10.1016/j.cirp.2016.04.054.
[29] L. Schild, L. Weiser, K. Höger, G. Lanza, Analyzing the error of Computed Tomography-based pore detection by using microscope images of matched cross-sections, Precis. Eng. 81 (2023) 192–206, https://doi.org/10.1016/j.precisioneng.2023.01.013.
[30] J.A. Slotwinski, E.J. Garboczi, K.M. Hebenstreit, Porosity measurements and analysis for metal additive manufacturing process control, J. Res. Natl. Inst. Stand. Technol. 119 (2014) 494–528, https://doi.org/10.6028/jres.119.019.
[31] J.M. Alegre, I.I. Cuesta, A. Díaz, Stress-intensity factor solutions for embedded elliptical cracks in round bars subjected to tensile load, Theor. Appl. Fract. Mech. 117 (2022), https://doi.org/10.1016/j.tafmec.2021.103189.
[32] M. Ji, H. Li, J. Zheng, S. Yang, Z. Zaiemyekeh, J.D. Hogan, An experimental study on the strain-rate-dependent compressive and tensile response of an alumina ceramic, Ceram. Int. 48 (19) (2022) 28121–28134, https://doi.org/10.1016/j.ceramint.2022.06.117.
[33] D. Kotsanis, P. Nomikos, and D. Rozos, "Comparison of Static and Dynamic Young's Modulus of Prasinites," p. 54, 2021, doi: 10.3390/materproc2021005054.
[34] W. de A. Thomaz, D. Y. Miyaji, and E. Possan, "Comparative study of dynamic and static Young's modulus of concrete containing basaltic aggregates," *Case Stud. Constr. Mater.*, vol. 15, 2021, doi: 10.1016/j.cscm.2021.e00645.
[35] A. Tridello, D. S. Paolino, and M. Rossetto, "Ultrasonic VHCF tests on very large specimens with risk-volume up to 5000 mm^3," *Appl. Sci.*, vol. 10, no. 7, Apr. 2020, doi: 10.3390/app10072210.
[36] "JIS R1601:2008 - Testing method for flexural strength (modulus of rupture) of fine ceramics at room temperature," *Japanese Ind. Stand./Japanese Stand. Assoc.* 2008.
[37] "E1820 − 21 - Standard Test Method for Measurement of Fracture Toughness," *ASTM Int.*, 2022, doi: 10.1520/E1820-20B10.1520/E1820-21.
[38] C. Hou, X. Jin, L. Zhao, P. Li, X. Fan, Analysis of tensile strength and fracture toughness of ZrB2 – SiC ceramic from three-point bending samples with edge cracks, Ceram. Int. 48 (20) (2022) 30078–30085, https://doi.org/10.1016/j.ceramint.2022.06.278.
[39] H. Salavati, H. Mohammadi, Y. Alizadeh, M.R. Ayatollahi, 3D fracture behaviour of graphite specimens weakened by V- notches with end holes under mixed mode (I+II) loading, Eng. Fail. Anal. 104 (2019), https://doi.org/10.1016/j.engfailanal.2019.06.050.